Granular Matter (2024) 26:38
https://doi.org/10.1007/s10035-024-01409-3

ORIGINAL REPORT

Effect of free water on the quasi-static compression behavior of partially-saturated concrete with a fully coupled DEM/CFD approach

M. Krzaczek[1] · J. Tejchman[1] · M. Nitka[1]

Received: 20 September 2023 / Accepted: 5 February 2024 / Published online: 9 March 2024

Abstract
The work aims to numerically investigate the quasi-static response of partially fluid-saturated concrete under two-dimensional uniaxial compression at the mesoscale. We investigated how the impact of free pore fluid content (water and gas) affected the quasi-static strength of concrete. The totally and partially fluid-saturated concrete behavior was simulated using an improved pore-scale hydro-mechanical model based on DEM/CFD. The fluid flow concept was based on a fluid flow network made up of channels in a continuous region between discrete elements. A two-phase laminar fluid flow was postulated in partially saturated porous concrete with very low porosity. Position and volumes of pores/cracks were considered to correctly track the liquid/gas content. In both dry and wet conditions, a series of numerical simulations were performed on bonded granular specimens of a simplified spherical mesostructure that mimicked concrete. The effects of fluid saturation and fluid viscosity on concrete strength and fracture, and fluid pore pressures were investigated. It was found that each of those effects significantly impacted the hydro-mechanical behavior of concrete. Due to the rising fluid pressure in pores during initial specimen compaction under compressive loading that promoted a cracking process, the compressive strength increased as fluid saturation and fluid viscosity decreased.

Keywords Concrete · Free water · Uniaxial compression · DEM-CFD · Strength · Fracture

1 Introduction

Water frequently comes into touch with concrete structures. Water may permeate through concrete because it is porous with many macropores, capillary pores, flaws, and cracks. This can have a significant impact on the static/dynamic mechanical properties of concrete because it affects the capillary tension, pore water pressure, inter-particle cohesion, and friction [1–4]. This results in the viscosity effect and meniscus stress of free water. Studying the impact of free water on the mechanical reaction of concrete is, therefore, crucial for the construction of concrete structures, e.g. hydraulics, marine engineering, bridges, and tunnels. Chemically bonded, physically bonded, and free water are the three forms of water that are generally present in concrete. It is a well-known fact that wet concrete materials perform substantially differently in laboratory trials under quasi-static loading conditions compared to dynamic loading ones [5–10]. Additionally, the greater the initial porosity of concrete, the higher the effect of water saturation on the strength [11, 12]. The mechanical properties of concrete with a high water–cement ratio are also more sensitive to water saturation than concrete with a low water–cement ratio. In general, the response of saturated concrete under loading is similar to that of mortars and rocks. The impact of the moisture variation in concrete during loading is typically ignored in practice.

Numerous quasi-static laboratory studies demonstrate that increasing water saturation causes a drop in compressive and tensile strength. In compression, the effect of water saturation is more pronounced than in tension. Concrete's fracture toughness, splitting tensile strength, and compressive strength all show an approximately linearly decreasing trend as water saturation rises [11, 13, 14]. The negative

✉ J. Tejchman
tejchmk@pg.edu.pl

M. Krzaczek
marek.krzaczek@pg.edu.pl

M. Nitka
micnitka@pg.edu.pl

[1] Faculty of Civil and Environmental Engineering, Gdansk University of Technology, Narutowicza 11/12, 80-233 Gdańsk, Poland

effect of water saturation on compressive strength is similar during both uniaxial and triaxial compression [15–17]. However, certain laboratory studies reveal that the strength and fracture toughness exhibit the characteristics of first decreasing and then increasing, and reflect a non-linear or bilinear relationship with the growth of the water saturation [18, 19]. In the case of elastic modulus of concrete, it usually increases [11, 20], does not much change [13], or decreases with a growing saturation ratio [21]. Water content is also one of the key elements influencing the material strain rate effect. Free water may even boost the dynamic compressive and tensile strength of cement-based materials when the strain rate rises to a specific point [11, 22–24]. There are many interpretations for the physical mechanism causing the reduced strength of wet concrete in quasi-static tests including e.g. the increase of an internal humidity gradient [11, 25] and the loosening of a molecular system in ITZs [13]. Some authors regarded the growth of pore pressure due to pore closure [26], and the water wedging in cracks [11] as the main reasons. The weakened cohesion and van der Waals forces between microscopic particles [13, 27] were also found to be the reasons for the strength drop. Finally, the effects of capillary suction [2, 19], viscosity [2, 28], viscous friction [28] and temperature-induced expansion [28, 29] were highlighted as the main reasons for the strength reduction. However, no explaining agreement has yet been achieved on this issue. It should be noted that there may be some inconsistency between the experimental results that are now available due to the various ways that dry and wet concrete are prepared [30].

Our research aims are to explain the behavior of wet concrete in compression and tension under quasi-static and dynamic conditions. The current study deals with quasi-static uniaxial compression of wet concrete only. It aims to (a) check the capability of a fully coupled DEM-CFD approach to realistically simulate the quasi-static mechanical behavior of partially saturated concrete specimens at the mesoscale, (b) explain the physical reason for the strength reduction in wet concrete specimens, and (c) demonstrate a quantitative impact of free fluid (water and gas) migration on both the concrete strength and a fracture process. The research examines how the mechanical effects of fluid on dry and wet concrete specimens modify the quasi-static mechanical properties of the material in compression. A fully coupled hydro-mechanical technique based on 2D DEM/CFD was adopted to investigate the solid–fluid interaction [31, 32]. The 3D DEM/CFD model is still in the testing phase, hence the 2D model was used. The model proposed takes into account the two-phase laminar flow of immiscible and compressible fluids. No external pressure is needed to move the fluid; it can be driven by local pressure changes resulting only from changes in pore volumes. Owing to this, the proposed model can realistically reproduce the interaction between flowing fluid and solids during compression tests.

The proposed improved DEM/CFD model employs a direct numerical simulation method. DEM was used to represent the mechanical behavior of concrete specimens by using discrete spherical elements interacting locally through normal and tangential contacts that generate cracks during their failure. There are several different discrete models for concrete mechanical behavior developed in the literature, such as classical lattice models, rigid-body-spring models, lattice discrete particle models and discrete element methods [33]. We chose DEM since it realistically captures the fracture processes in concrete [34–38]. Additionally, it correctly depicts mesostructure and contact forces, using simple dynamic equations. Using CFD, a flow network made up of predefined channels was used to represent the laminar viscous two-phase fluid flow (water and gas) through pores and cracks in a continuous domain between the discrete elements. Calculations in isothermal conditions were performed in this research stage on 2D small-size bonded granular specimens of a simplistic mesostructure resembling concrete under uniaxial compression. Concrete was treated as a one-phase material only, composed of bonded spheres with different diameters without distinguishing aggregate, mortar, ITZs, and macro-pores [35, 37]. Additionally, there was a relatively low number of spheres and a narrow range of particle diameter sizes. Therefore, the mechanical concrete behavior (stress–strain curve and fracture process) in laboratory tests was approximately reproduced. The main attention was focused in the paper on the effect of pore fluid migration and pressure on the specimen's compressive strength. In a series of DEM/CFD simulations, the different fluid saturation and fluid viscosity were the variables that were explored.

The capillary pressure, defined as the difference between the partial pressures of two phases: the wetting phase (water) and non-wetting phase (water vapor or moist air), was neglected in the current DEM analyses for the sake of simplicity. According to this definition, when the concrete is fully saturated, there is no capillary flow. In partially saturated concrete, capillary flow can occur even when there is no external fluid source (due to the flow of viscous fluid during compression). The flow of the liquid phase can fill in some capillaries with water to the point where the snap-off mechanism [39, 40] is activated. Even if capillaries are not filled in with water, this mechanism immediately fills them with water. When the capillary is filled in with water, the typical capillary flow may begin (a piston-like mechanism). The capillary pressure can reach even 1.5 MPa (and more) and strongly depends upon the initial saturation and size and number of capillaries. However, its impact is solely local. Capillary pressure and capillary flow mechanisms were implemented in the proposed DEM-CFD model [41]. The

influence of capillary pressure on the compressive strength of wet concrete will be investigated in the next phase of the research.

Several coupled hydro-mechanical DEM-CFD models have been suggested in the literature (e.g. [42–57]). The review of those DEM-based coupled models was given in [31]. As compared to those models, the DEM/CFD-based mesoscopic method for fluid flow in partially fluid-saturated porous cohesive-frictional materials with very low porosity that is presented in the current study has several advantages such as.

(1) The direct numerical simulation approach is used to solve fluid flow equations in a two-dimensional continuous fluid domain between discrete elements.
(2) The fluid and discrete domains of solids reside in one physical system. Both domains are discretized into one triangular mesh.
(3) Due to the triangular mesh in the fluid domain, the variable geometry, size, position, and volume of pores/cracks are considered to correctly track the liquid/gas content. Hence, the effect of material skeleton deformation on the fluid pressure distribution can be studied.
(4) An effective method is developed to automatically mesh and re-mesh these domains to account for changes in the geometry and topology of particle and fluid domains.
(5) Coarse meshes of solid and liquid domains are utilized to build a virtual fluid flow network (VPN).
(6) The two-phase immiscible fluid contains both a liquid (water) and a gas (water vapor or moist air).

There also exist hydro-mechanical models, based on lattice and lattice discrete particle models [58–63]. The models are simplified since the pore fluid pressure does not depend on volume changes which are ignored. The fluid flow is solely caused by external fluid pressure or relative humidity difference. However, during compression, the fluid flow is mainly driven by changes in pore pressures, which are affected by changes in pore volumes.

The impact of free water content on the response of concrete under various stress levels and static/dynamic loading situations was investigated using several numerical coupled models. Most of these simulations were done within continuum mechanics (e.g. [64, 65]). DEM solutions also exist for this problem (e.g. [66]); they are approximations since they do not take into consideration the true coupling between solid (DEM) and fluid mechanics (CFD).

This article is a follow-up to the authors' prior mesoscopic numerical investigations, which employed a fully coupled DEM-CFD model to numerically analyze hydraulic fracturing in rocks [31, 32] and hydraulic/capillary flow in unsaturated mortars and concretes [41]. With thorough 3D CFD simulations using the Reynolds-averaged Navier–Stokes equations in the continuous domain between particles, the coupled DEM/CFD technique was validated [67, 68]. It was demonstrated that the turbulent kinetic energy and turbulent dissipation energy are relatively low and may be disregarded in the simplified fluid flow model. Heat transfer has recently been added to the authors' coupled DEM/CFD model [69, 70].

The structure of the current paper is as follows. After the introduction in Sect. 1, Sect. 2 provides a mathematical model of the DEM/CFD-based coupled hydro-mechanical technique. Section 3 describes the input data for DEM-CFD simulations. Pure DEM simulation results are gathered in Sect. 4. Section 5 displays several numerical simulation results with DEM-CFD on the behavior of fully and partially saturated concrete under uniaxial compression. Section 6 contains some concluding remarks. The YADE open-source software program [71, 72] was enhanced by the authors to include the fully coupled DEM-CFD approach for partially saturated bonded granular materials.

2 Two-dimensional DEM/CFD-based model

In [31] and [32], the coupled DEM-CFD model was thoroughly explained. For the sake of clarity, Sect. 2 only contains the model's most crucial details. The direct numerical simulation (DNS) approach is used to solve fluid flow equations in a two-dimensional continuous fluid domain between discrete elements (unlike existing fluid flow models).

2.1 DEM for cohesive-frictional materials

DEM simulations are carried out using the 3D explicit solver of discrete element open-source software YADE [71, 72]. With the use of Newton's second law of motion and an explicit time-stepping method, particles in a DEM interact with one another during translational and rotational motions [73]. At the grain contact, the model suggests a cohesive bond with a brittle failure below the critical normal tensile force. Under usual compression, shear cohesion failure causes contact slip and sliding, which are controlled by the Coulomb friction law. The basic governing equations of DEM are presented in Appendix A (Eqs. A1–A7) [34–38]. Non-viscous damping is chosen [74] (Eq. A7) in simulations to speed up convergence. In DEM, an arbitrary microporosity may be attained due to the possibility of particle overlap. The following material constants are required for DEM simulations: E_c, υ_c, μ_c, C, and T (Appendix A). Additionally necessary are the parameters R (sphere's radius), ρ (mass density), and α_d (damping factor). The damping factor

is consistently set to $\alpha_d = 0.08$ [35]. The particle contact ratio *C/T* must be carefully taken into account to properly simulate the distribution of shear and tensile cracks, the relationship between the uniaxial compressive and tensile strength, and the failure mode of specimens (brittle or quasi-brittle) [75].

The process of running several DEM simulations and comparing the results to experimental data from simple tests, such as uniaxial compression, triaxial compression, and simple shear, is typically used to determine the material constants. The DEM model does not account for material softening. The model has been successfully employed by the authors in the modeling of engineering particulate materials, primarily granular materials [76–79], concretes [34–38, 80, 81], and rocks [32, 75]. The grain damage was not considered in current DEM simulations. This process may be easily taken into account in DEM simulations (by using collections of particles to represent the grains allowing for intra-granular fracture), although their time will be much increased. A shortcoming of DEM is the huge time of computation in industrial-scale problems.

2.2 Fluid flow model

A fundamental idea for streamlining the fluid flow model was put forth in [31] and [32]. The 2D DEM-CFD model developed by the authors is based on the idea that two domains coexist in a physical system: a discrete 3D domain (solid) and a continuous 2D domain (fluid) (Fig. 1). This is in contrast to the basic concept of usual fluid flow networks. It was assumed that the discrete domain was originally 3D due to the need to use a 3D DEM solver in YADE software. Consequently, the initially fluid domain is two-dimensional, while the solid domain consists of a single layer of discrete 3D elements (spheres). The centers of gravity of discrete elements are positioned on a plane (2D surface). To transform discrete 3D elements into a 2D problem, the discrete elements are then projected onto a plane to create circles, which are then discretized into a 2D triangular mesh along with voids [31] (Fig. 1). Finally, after projection and discretization, there are two 2D domains: the fluid domain and the solid domain. Note that the displacement of the spheres in the OZ direction (perpendicular to the plane) is fixed. Therefore, although the 3D DEM solver in YADE is used, the mechanical problem is quasi 2D as in the fluid flow model. In the CFD model, all definitions regarding the geometry of both domains (solid and fluid) are treated as two-dimensional, and the third dimension has a unit size.

In the 2D fluid domain, the centroids of the triangles are connected by channels and form a fluid flow network. To get a more precise distribution of pressures, fluid-phase fractions, and densities, a remeshing technique discretizes the overlapping circles, sets the contact lines, and eliminates the overlapping areas [31, 32]. The contact forces are estimated based on the pressure and shear stress for the specimen thickness equal to the mean particle diameter. The basic equations of the fluid flow model are given in Appendix B (Eqs. B1–B28). The mass change in triangular cells is correlated with the density change in a fluid phase, which results in changes in pressure. Because of this, triangles do not obey the equation for the conservation of momentum, but their mass is nevertheless conserved throughout their whole volume. This procedure is carried out using an explicit formulation for every VP in the fluid flow network, called a Virtual Pore Network (VPN). Initially, the liquid and gas might be present in the material and pre-existing discontinuities. Two distinct channels are introduced by VPN [31]:

(A) Artificial 'S2S' channels are those that connect discrete concrete elements that are in contact with one another and
(B) Actual 'T2T' channels are those that link grid triangles in pores that are in contact with one another along a common edge.

The channel length is thought to be the distance between the gravity centers of adjacent grid triangles. The mass flow rate in channels is calculated by solving continuity and momentum equations for laminar flows of an incompressible fluid. The fluid flow in the network only serves to estimate the fluid's mass flow rate as it passes through the triangle cell's face (edge).

Three flow regimes are identified in the channels [31]: (a) single gas phase flow with a gas phase fraction, (b) single liquid phase flow with a liquid phase fraction, and (c) two-phase flow (liquid and gas). In the flow regime (a) and (b) (single phase fluid flow) the Poiseuille equation [82, 83] is used to compute the mass flow rate. The two-phase fluid flow driven by a pressure gradient in adjacent VPs exhibits similar behavior to a two-phase fluid flow of two immiscible and incompressible fluids in channels (Fig. 2).

The gas phase fraction and the liquid phase fraction are denoted by the symbols α_p and α_q, respectively, and they sum to 1. They are local parameters of the single cell in the mesh. When defining the initial conditions, the parameters can be the same for each grid cell. The liquid–gas interface is parallel to the channel plates and is calculated as the average of the liquid phase fraction in adjacent cells. However, the fraction of liquid and gas phases changes over time, as well as the position of the phase interface in the channel. Gravity's effects are disregarded. While the volumetric flow rates of the fluid phases are unknown, the interface position is connected to fractions of the fluid phases in adjacent VPs. Equations of continuity and momentum describe the flow in each phase.

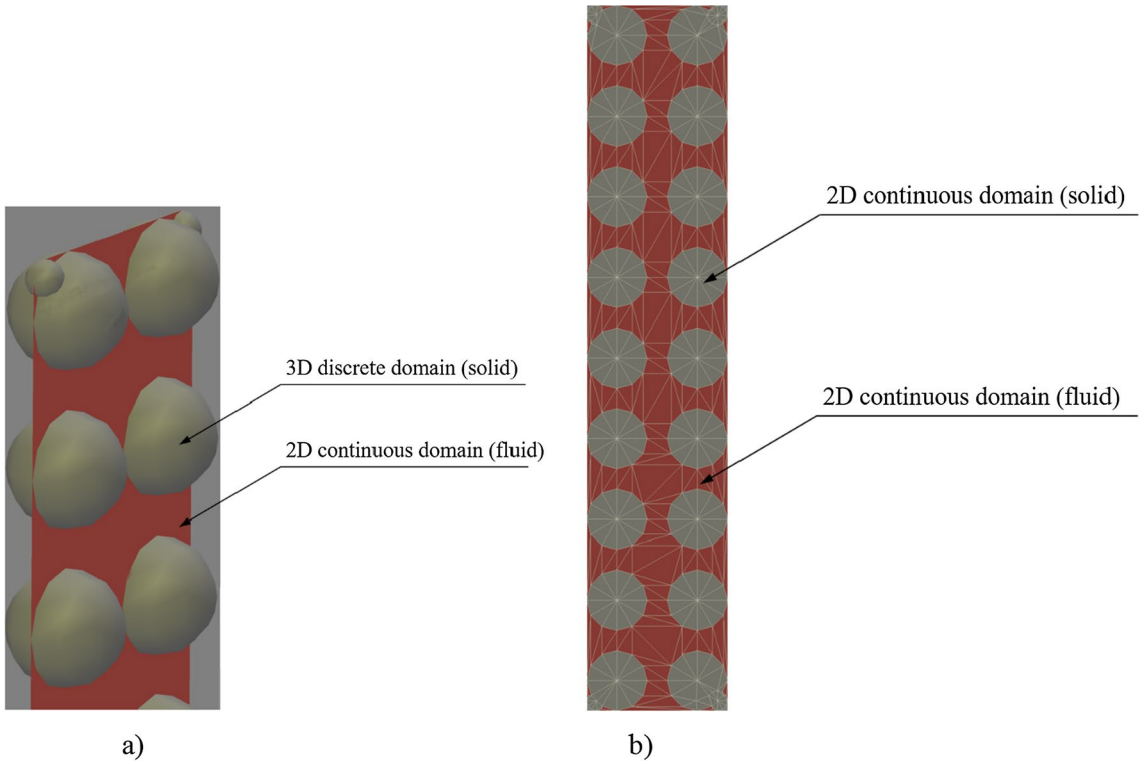

Fig. 1 Two domains co-existing in one physical system: **a** domains before projection and discretization and **b** solid and fluid domains after discrete elements projection and discretization (fluid domain is in red and solid domain is in grey) [31] (colour figure online)

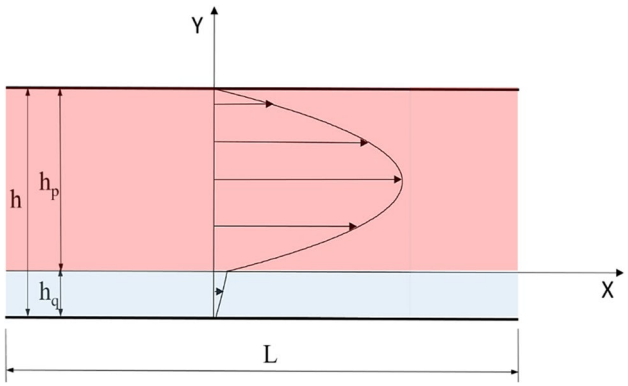

Fig. 2 Two-layer fluid flow in channels 'S2S' and 'T2T' (*h*—channel aperture, *L*—channel length, '*q*'—liquid and '*p*'—gas) [32]

VPs, unlike the channel flow model, assume that the fluid is compressible, which means that the density of the fluid phases can change in space and time. The fluid pressure can reach 70 MPa in specific situations, such as during the hydraulic fracturing process. The gas phase exceeds the critical point and becomes a supercritical fluid under these conditions. Therefore, for both fluid phases in VPs, the Peng-Robinson equation of state [69] is used to describe fluid behavior. Assuming that both fluid phases have the same pressure (as in the Euler model), the pressure equation is solved to determine the density of the fluid phase. The mass conservation equation for both phases is applied to compute the density of the liquid/gas phase. Finally, the cell pressure (VP) is calculated from the Peng-Robinson equation of state. The basic equations of the fluid flow model in pores (VP) are given in Appendix B (Eqs. B10–B28).

Four major phases make up the numerical algorithm:

(a) by resolving momentum and continuity equations, one can calculate the mass flow rate for each phase of fluid flowing through the cell faces (in channels encircling VP),
(b) using equations of state and continuity to calculate the phase fractions and their densities in VPs,
(c) utilizing the equation of state to determine the pressure in VPs,
(d) updating material properties (e.g. liquid and gas densities in each cell grid).

3 Input data for 2D DEM/CFD simulations

Typically, mechanical (DEM) and permeability and sorptivity tests (CFD) are used to calibrate DEM and CFD separately [31, 32, 41]. For the numerical calculations in

the first calculation stage, a simple one-phase model for concrete made out of spheres with varying diameters was employed to roughly depict quasi-static concrete's performance in uniaxial compression as compared to laboratory tests. The diameters of spheres d were arbitrarily set to range from 1.0 to 1.8 mm, with a mean diameter of $d_{50}=1.4$ mm. For uniaxial compression tests with dry and wet specimens (containing about 1600 spheres), a quadratic specimen of 50×50 mm^2 was assumed (see Fig. 4, Sect. 4). The specimen thickness was always equal to the mean grain diameter. Horizontal boundaries at the top and bottom were frictionless and smooth. Vertical boundaries were free to move. One grain at the bottom midpoint was fixed. A continuous lowering of the top specimen boundary caused deformation in the specimen. There were no pre-existing macropores or cracks in the specimen. The initial micro-porosity was $p=5\%$ (being equivalent to typical concrete [37, 81]). The stress–strain curve and the deformed specimen are presented in Figs. 3 and 4 of Sect. 4. The estimated compressive strength (36 MPa), the corresponding vertical normal strain (0.23%), the elastic modulus (20 GPa), and the crack pattern are in agreement with the experimental ones for usual concrete [84]. The more realistic response of concrete due to uniaxial compression, described as a four-phase material at the mesoscale, was shown in [37].

For permeability simulations with pure CFD, a quadratic non-deformable specimen of 10×10 mm^2 was chosen as in [41]. The macroscopic permeability coefficient κ of the concrete specimen, calculated with Darcy's law, was 4.0×10^{-16} m^2 for the values of h_{inf}, h_0, γ, and β (Eqs. B1 and B2 in Appendix B) given in Table 1 [41]. This value is in agreement with experimental results for concretes and mortars [41]. The larger values of h_{inf}, h_0, γ, and β caused the permeability coefficient κ higher. An arbitrary permeability coefficient may be, thus, assumed in numerical calculations.

The basic material constants assumed for concrete specimens in the coupled DEM-CFD calculations are given in Table 1. The adaptive time step in DEM and CFD was always defined [31]. The maximum time step was limited to $1\cdot10^{-8}$ s. The computation time of one simulation was about 14 h on a computer with two Intel Xeon Platinum processors 8280 (2.70 GHz). The computational cost of the simulation was relatively high because the existing DEM-CFD model was parallelized on threads only but not in a distributed mode (on cluster computer nodes).

4 Pure DEM simulation results

The specimen 50×50 mm^2 was assumed for mechanical computations (Sect. 3). In Figs. 3, 4, 5, 6 and 7, DEM's numerical findings for concrete defined as a one-phase material, composed of spheres with diameters of 1.0–1.8 mm (without distinguishing aggregate, mortar, ITZs, and macropores [36–38]), are displayed in uniaxial compression. Figure 3 illustrates the stress–strain diagram. On the diagram, some of the characteristic points '1'– '6' were marked. Figures 4 and 5 show the progression of the fracture patterns and broken particle contacts (marked by lines tangential to the contact surfaces) for the various vertical normal strains (points 1–6). The development of the relative broken contact number is depicted in Fig. 6. Figure 7 shows the distribution of the compressive and tensile contact forces at the maximum vertical normal stress (point '5' in Fig. 3).

For a vertical normal strain of $\varepsilon_y=0.235\%$, the estimated compressive strength was $f_c=36$ MPa and the elastic modulus was $E=20$ GPa (Fig. 3). The elastic range was up to $\varepsilon_y=0.11\%$. Due to several simplifications assumed in the calculations to accelerate the simulations (e.g. one-phase material composed of spheres, narrow particle diameter size range, a small number of spheres, and 2D conditions), the stress–strain curve was solely approximately reproduced. The calculated specimen's pre-peak response was too linear and its post-peak response was too brittle (Fig. 3). Without those 3 first simplifications, the concrete behavior (stiffness, strength, brittleness, and fracture) can be realistically reproduced in simulations of uniaxial compression [37, 38]. Jumps on the stress–strain curve in Fig. 3 were caused by crack formation. A few almost vertical cracks that appeared during uniaxial compression were the failure mode (Figs. 4 and 5). Long before the peak stress, at around $\varepsilon_y=0.0582\%$, the first micro-cracks occurred in the specimen (Fig. 6). More than 25% of contacts were already damaged at the maximum vertical stress ($\varepsilon_y=0.235\%$). The rate of contact damage progressively rose during compression. After the peak stress for $\varepsilon_y>0.235\%$, it reached its maximum rate (Fig. 6). A network of vertical normal contact forces

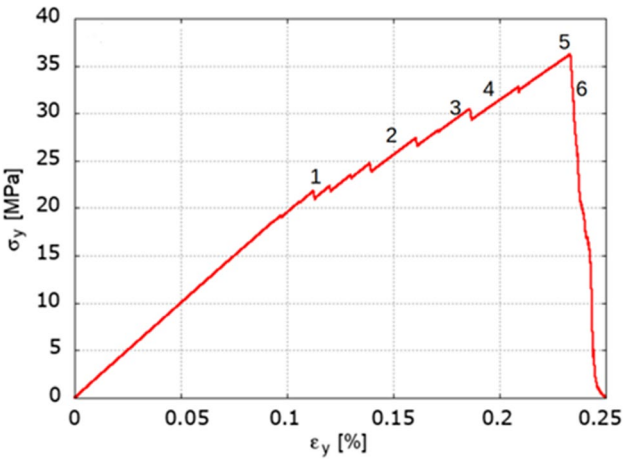

Fig. 3 Pure DEM simulation results for one-phase concrete specimen during uniaxial compression-relationship between vertical normal stress σ_y and vertical normal strain ε_y with marked characteristic points 1–6

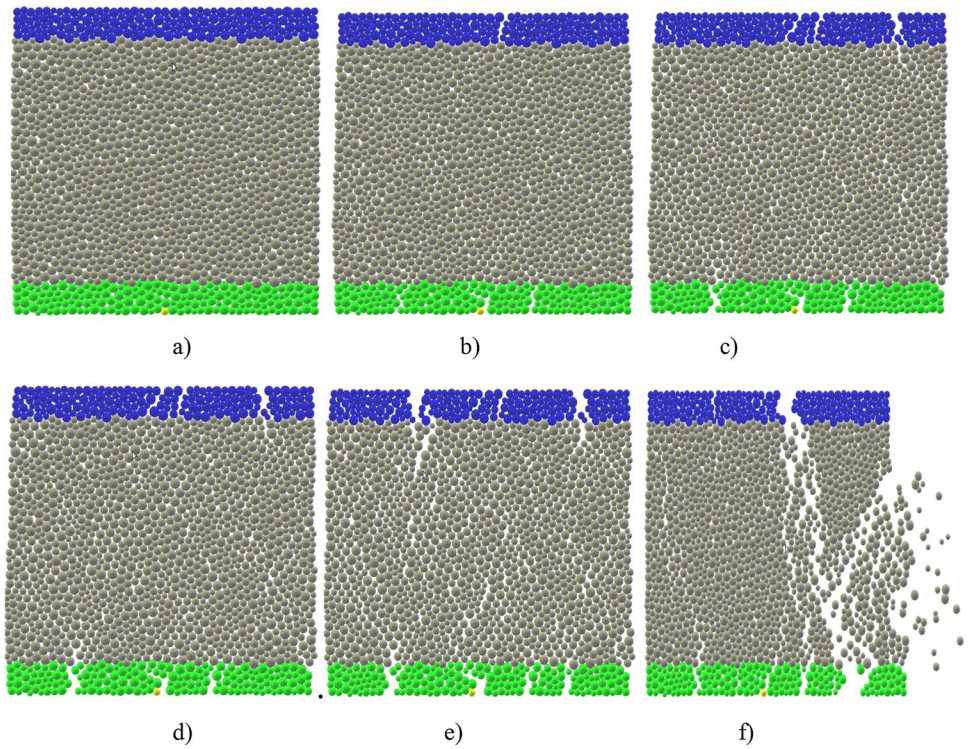

Fig. 4 Pure DEM simulation results for one-phase concrete specimen during uniaxial compression: evolution of fracture pattern **a** $\varepsilon_y = 0.12\%$, **b** $\varepsilon_y = 0.15\%$, **c** $\varepsilon_y = 0.18\%$, **d** $\varepsilon_y = 0.19\%$, **e** at peak stress ($\varepsilon_y = 0.235\%$), and **f** slightly after peak stress (blue particles have constant vertical velocity and green particles are blocked in vertical direction, displacements are magnified by factor 30) (colour figure online)

Table 1 Basic material constants assumed for concrete, fluid and gas in DEM/CFD calculations

Material constants for concrete	Symbol	Value	Unit
Modulus of elasticity of contact (Eq. A3)	E_C	27	(GPa)
Poisson's ratio of contact (Eq. A3)	υ_c	0.2	(–)
Cohesion at contact (Eq. A6)	C	120	(MPa)
Tensile strength of contact (Eq. A6)	T	24	(MPa)
Inter-particle friction angle (Eq. A4 and A5)	μ_c	18	(°)
Mass density (Sec. 2.1)	ρ	2600	(kg/m^3)
Damping factor (Sec. 2.1)	α	0.08	(–)
Initial porosity (Sec. 2.1)	p	5.0	(%)
Material constants for fluid (water)			
Dynamic viscosity (Eq. B4)	μ_q	$10.02 \cdot 10^{-4}$ or $5.01\ 10^{-4}$	(Pa s)
Initial fluid volume fraction (Eq. B8)	α_q	1.0 or 0.7 or 0.3	(–)
Molecular weight (Eq. B22)	wq	18.01528	(kg/kmol)
Material constants for gas			
Dynamic viscosity (Eq. B4)	μ_p	$2.0507 \cdot 10^{-5}$	(Pa s)
Molecular weight (Eq. B21)	w_p	28.9647	(kg/kmol)
Universal gas constant (Eq. B10)	R	8.31	(J/(mol K))
Initial gas volume fraction (Eq. B8)	α_p	0 or 0.3 or 0.7	(–)
Fluid flow network parameters			
Channel width (Eq. B1)	h_{inf}	$4.5 \cdot 10^{-7}$	(m)
Channel width (Eq. B1)	h_0	$3.25 \cdot 10^{-6}$	(m)
Aperture coefficient (Eq. B1)	β	1.0	(–)
Reduction factor (Eq. B2)	γ	0.012	(–)

conveyed the external vertical load (Fig. 7a). Too weak tensile contact forces led to specimen damage (Fig. 7b).

5 DEM/CFD simulation results

The same concrete specimen 50×50 mm^2 was assumed for hydro-mechanical computations. The initial fluid (water and gas) pressure in the specimen was $P_o=0.1$ MPa. The impact of various initial fluid volume fractions α_q ($\alpha_q=0.3$, 0.7, and 1.0) on the stress–strain curve during uniaxial compression is shown in Fig. 8.

The numerical results demonstrate that when the initial fluid volume fraction α_q increased, the compressive strength f_c and the related vertical normal strain ε_y decreased. The reduction of f_c with increasing fluid volume fraction α_q was approximately linear, agreeing with experiments [11, 13, 14]. The initial material stiffness remained the same up to $\varepsilon_y=0.1\%$ due to low pore fluid pressures (see Fig. 18a) caused by low specimen porosity [30] and the lack of cracks. This numerical outcome is in agreement with the experiment in [13] but contrasts with some laboratory tests wherein the elastic modulus rose [11, 20] or declined [21] with a higher saturation degree. In comparison to the results for a dry specimen ($\alpha_q=0$) (curve 'a' in Fig. 8), the vertical normal strain was 20% lower for a fully saturated specimen ($\alpha_q=1.0$) and the compressive strength was 15% lower. Due to the initial porosity's low value of 5%, those reductions were relatively small for the wet specimen [11, 30]. For a partially saturated specimen, the brittleness was slightly higher. The curves $\sigma_y=\mathrm{f}(\varepsilon_y)$ had a similar shape regardless of α_q.

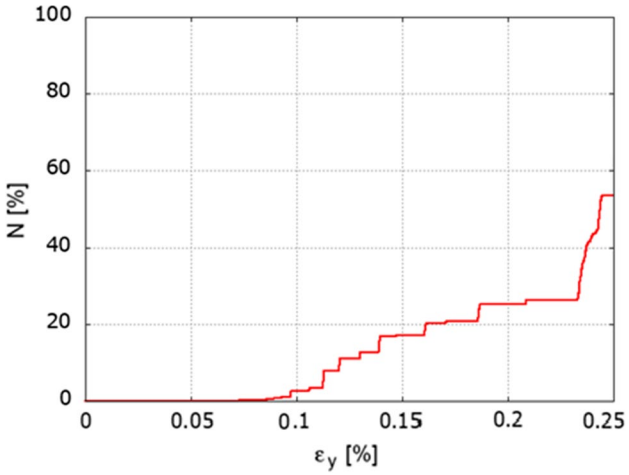

Fig. 6 Pure DEM simulation results for one-phase concrete specimen during uniaxial compression: evolution of relative number N of broken contacts in (%)

5.1 Mechanical results for wet specimens

For the fully fluid-saturated specimen ($\alpha_q=1.0$), the DEM-CFD findings are given in Figs. 9, 10, 11 like the pure DEM results (Figs. 4, 5, 6). The developments of the fracture patterns and broken contacts are illustrated in Figs. 9 and 10.

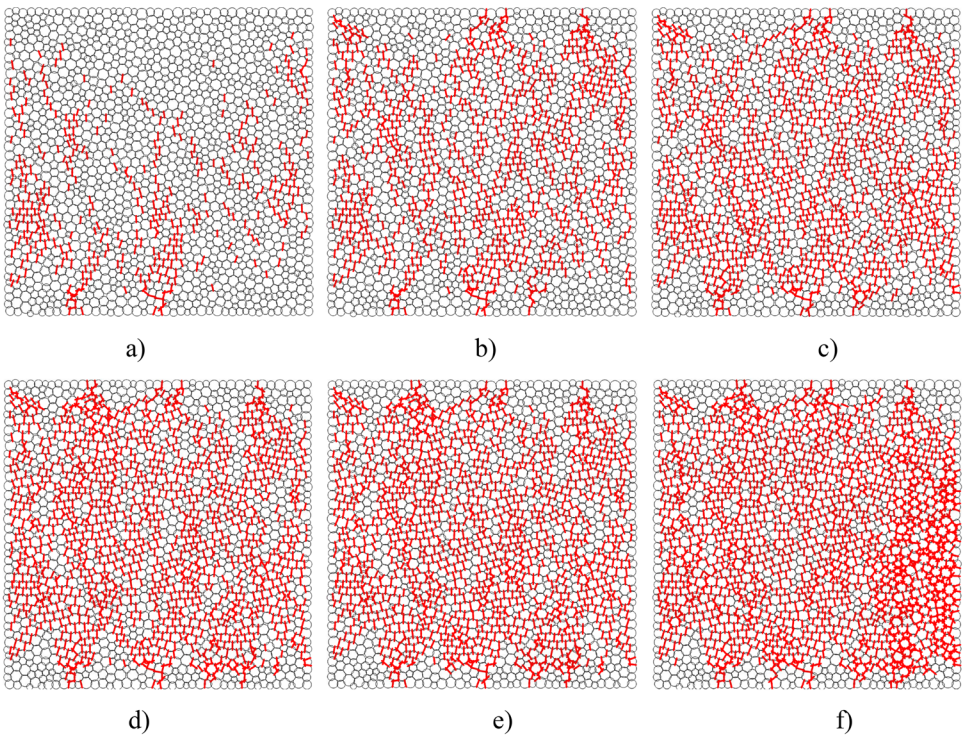

Fig. 5 Pure DEM simulation results for one-phase concrete specimen during uniaxial compression: distribution of broken contacts (marked by lines tangential to contact surfaces) in non-deformed specimen for different vertical normal strain ε_y **a** $\varepsilon_y=0.12\%$, **b** $\varepsilon_y=0.15\%$, **c** $\varepsilon_y=0.18\%$, **d** $\varepsilon_y=0.19\%$, **e** $\varepsilon_y=0.235\%$ (at peak stress), and **f** slightly after peak stress (broken contacts are marked in red) (colour figure online)

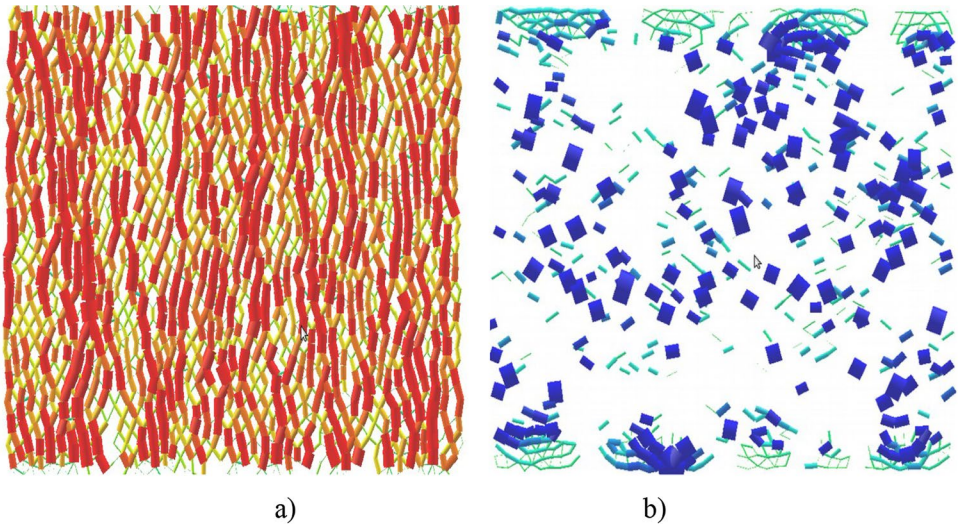

Fig. 7 Pure DEM simulation results for one-phase concrete specimen during uniaxial compression: distribution of contact forces at peak stress ($\varepsilon_y = 0.235\%$) **a** compressive forces and **b** tensile forces (force thickness denotes force magnitude)

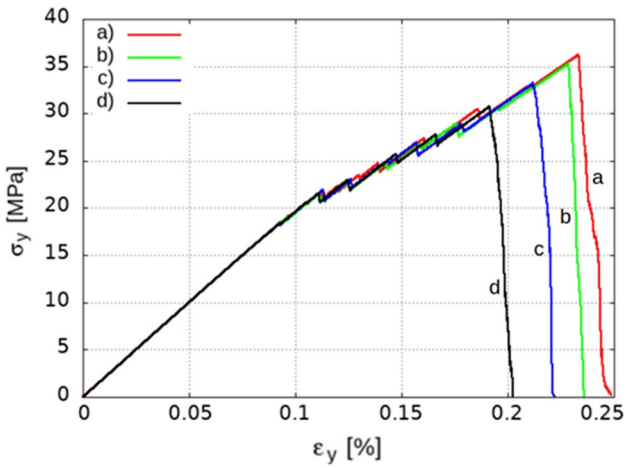

Fig. 8 Pure DEM and coupled DEM-CFD simulation results for one-phase concrete specimen during uniaxial compression with different initial fluid volume fraction α_q: relationship between vertical normal stress σ_y and vertical normal strain ε_y: **a** pure DEM (Fig. 3), **b** DEM-CFD with $\alpha_q = 0.3$, **c** DEM-CFD with $\alpha_q = 0.7$ and **d** DEM-CFD with $\alpha_q = 1.0$

Figure 11 shows how the damaged contact number changed over specimen deformation.

The wet specimen's behavior mirrored that of the dry specimen (Figs. 4 and 5). However, the wet specimen was slightly more damaged for $\varepsilon_y = 0.19\%$ and more and more damaged after the peak stress (Figs. 9, 10, 11) than the dry specimen. The first microcracks appeared a little bit earlier in the wet specimen as compared to the dry specimen ($\varepsilon_y = 0.0578\%$ versus $\varepsilon_y = 0.0582\%$) (Fig. 11).

Figures 12 and 13 present some results for the partially fluid-saturated specimen ($\alpha_q = 0.7$): the development of the fracture patterns (Fig. 12) and the evolution of broken contacts (Fig. 13). The wet specimen's behavior with $\alpha_q = 0.7$ and $\alpha_q = 1.0$ was similar, however, the specimen with $\alpha_q = 0.7$ was less damaged than this with $\alpha_q = 1.0$.

5.2 Fluid flow results for fully saturated specimen

The distributions of the high (> 0.1 MPa—initial pore fluid pressure) and low pore fluid pressure (≤ 0.1 MPa—initial pore fluid pressure) in the fully saturated specimen ($\alpha_q = 1.0$) are shown in Figs. 14, 15, 16 for a vertical normal strain $\varepsilon_y = 0.05\%$ (Fig. 14), $\varepsilon_y = 0.10\%$ (Fig. 15) and $\varepsilon_y = 0.19\%$ (peak stress) (Fig. 16). Figure 17 shows the distribution of pore fluid velocities in the specimen for a vertical normal strain $\varepsilon_y = 0.5\%$ (Fig. 17a), $\varepsilon_y = 0.10\%$ (Fig. 17b) and $\varepsilon_y = 0.19\%$ (peak stress) (Fig. 17c). The evolutions of the average and maximum pore fluid pressures during uniaxial compression are depicted in Fig. 18. Figure 19 depicts the evolution of fluid pressure in one arbitrary pore.

The specimen's pore fluid pressure distribution in the pores was noticeably non-uniform (Figs. 14, 15, 16). There were large areas with high fluid pore pressure (> 0.1 MPa—initial pore fluid pressure) and a few with low fluid pore pressure (≤ 0.1 MPa—initial pore fluid pressure). Different velocities of fluid flow were observed in the specimen (Fig. 17). The maximum pore fluid velocity was found to be 0.012 m/s (Fig. 17) and its location matched the location of the maximum fluid pressure.

The average fluid pore pressure initially increased due to the specimen compaction induced by a compression process and then reached an asymptote (Fig. 18a). Its maximum value was about 0.12 MPa. However, the maximum fluid pore pressure initially increased, then decreased and reached an asymptote (Fig. 18b). There were two small fluid pressure peaks around the vertical strain of 0.13% (Fig. 18b). They were caused by a momentary increase in sphere overlap, which resulted in a transient decrease in pore volume

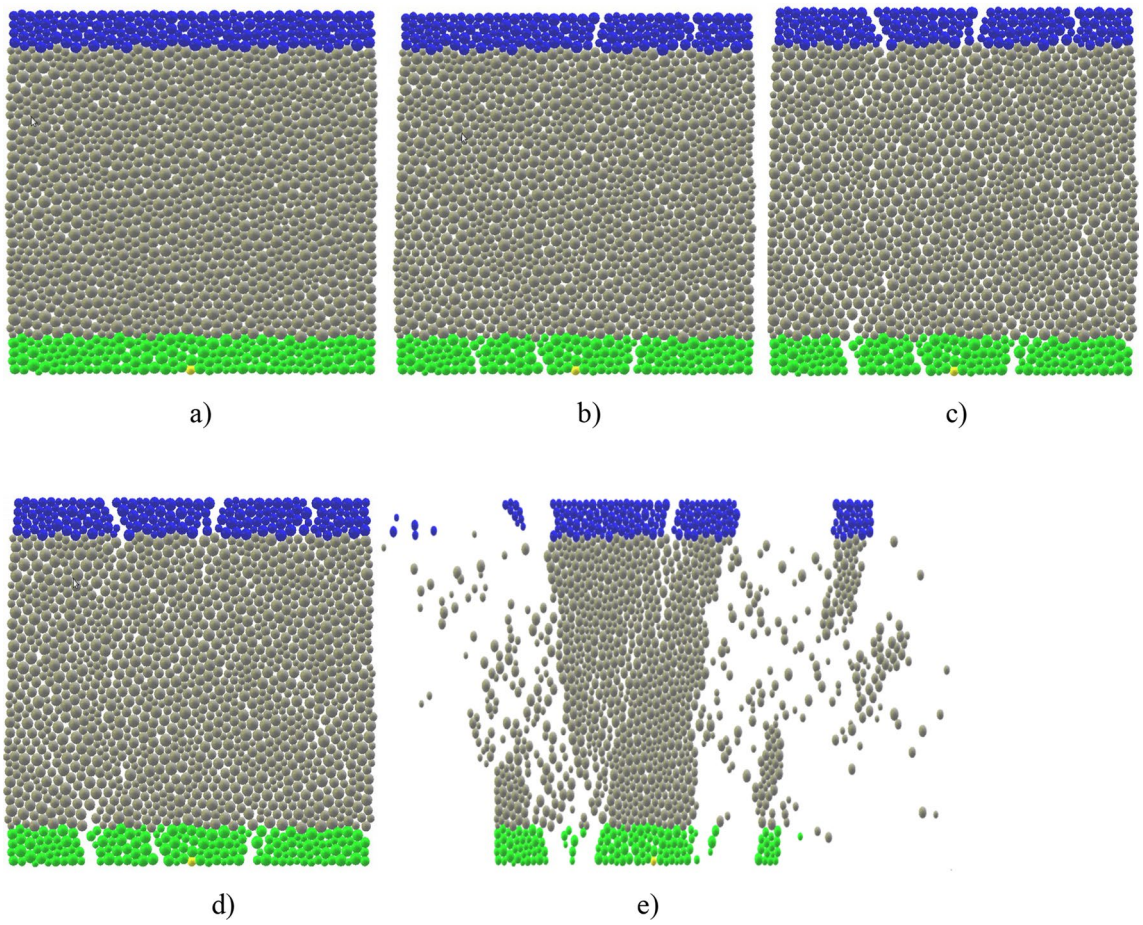

Fig. 9 DEM-CFD simulation results for one-phase concrete specimen ($\alpha_q = 1.0$) during uniaxial compression: evolution of fracture pattern **a** $\varepsilon_y = 0.12\%$, **b** $\varepsilon_y = 0.15\%$, **c** $\varepsilon_y = 0.18\%$, **d** at peak stress ($\varepsilon_y = 0.19\%$) and **e** slightly after peak stress (displacements are magnified by factor 30)

and an increase in fluid pressure. The maximum pore fluid pressure was locally about 0.8 MPa for $\varepsilon_y = 0.05\%$. Later, as microcracks started to appear in the specimen, the maximum pore fluid pressure lowered (down to 0.2 MPa). The biggest decline in pore fluid maximum pressure was seen in the region of $\varepsilon_y = 0.05$–0.085% (Fig. 18b). The fluid pressures were greater than the initial one equal to 0.1 MPa in the entire ε_y-range. Some suction pressures were noticeable in the specimen at some places (Figs. 14 and 19). The expansion of the crack intensity by the pore fluid pressure's increase over the initial one reduced compressive strength for wet specimens.

The increase of fluid pressure to the maximum value (during the entire simulation) was observed only in one pore (point 'P1' in Fig. 19a). Moving away from this point (e.g. point 'P2' in Fig. 19a), the maximum fluid pressure decreased and the changes in pressure over time smoothed out. This phenomenon was caused by a random arrangement of discrete elements. The movement in the uniaxial compression test caused discrete elements located along the upper edge of the specimen to move in different directions. By chance, the two spheres began to overlap. Consequently, the volume of pores located between these spheres began to decrease relatively quickly increasing fluid pressure. This effect was local, and the pressure of the fluid surrounding the pore decreased very quickly (Fig. 19b) at the same time step. The maximum fluid pressure at point 'P1' occurred slightly earlier (for vertical normal stress $\varepsilon_y = 0.0564\%$) than at point 'P2' (for vertical normal stress $\varepsilon_y = 0.066\%$). While the increase in fluid pressure at point 'P1' was caused by the deformation of the material skeleton, the increase in fluid pressure at point 'P2' was mainly caused by the flow of fluid from point 'P1' (higher pressure) to point 'P2' (lower pressure). The fluid flow took some time to increase the fluid pressure at P2 to its maximum value.

The material response was similar in other DEM-CFD results with a partially saturated specimen for the two various initial fluid volume fractions α_q ($\alpha_q = 0.3$ and 0.7). The average fluid pressure was around 0.102 MPa ($\alpha_q = 0.7$) (Fig. 20) and 0.1001 MPa ($\alpha_q = 0.3$). The maximum local fluid pressure was around 0.4 MPa ($\alpha_q = 0.7$) and 0.15 MPa ($\alpha_q = 0.15$). The compressive strength increased as α_q

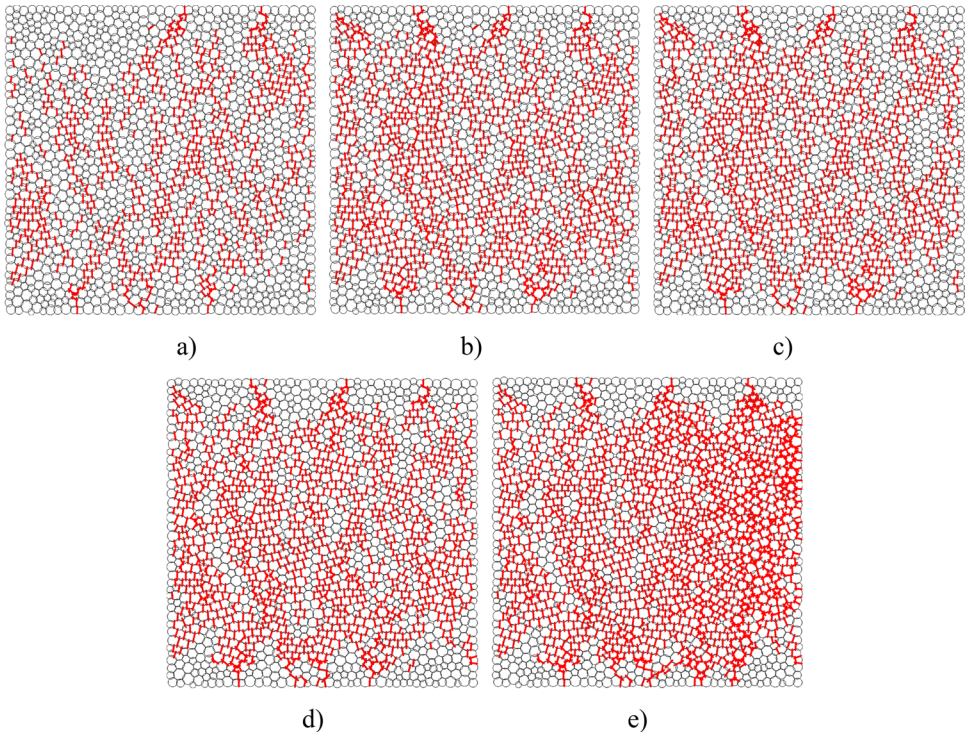

Fig. 10 DEM-CFD simulation results for one-phase concrete specimen ($\alpha_q = 1.0$) during uniaxial compression: distribution of broken contacts (marked by lines tangential to contact surfaces) in non-deformed specimen for different vertical normal strain ε_y **a** $\varepsilon_y = 0.12\%$, **b** $\varepsilon_y = 0.15\%$, **c** $\varepsilon_y = 0.18\%$, **d** at peak stress ($\varepsilon_y = 0.19\%$) and **e** slightly after peak stress (broken contacts are marked in red) (colour figure online)

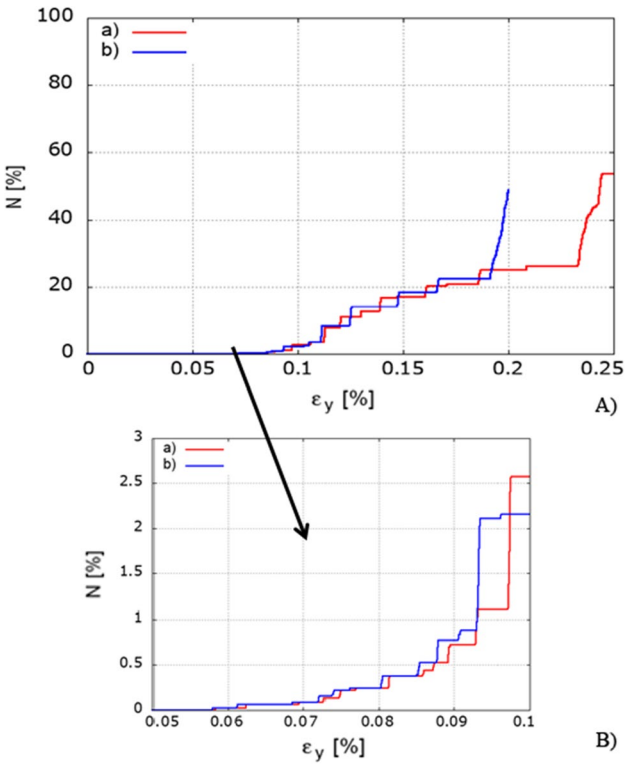

Fig. 11 Pure DEM (curve 'a') and coupled DEM-CFD simulation result (curve 'b') for one-phase concrete specimen (with $\alpha_q = 1.0$) during uniaxial compression: **A** evolution of relative number N of broken contacts with vertical normal strain ε_y and **B** zoom on onset of contact breakage

declined. The flow velocity also diminished with decreasing α_q.

5.3 Effect of viscosity

In the scenario with fully fluid-saturated concrete ($\alpha_q = 1$), the impact of viscosity μ_q on the stress–strain curve is illustrated in Fig. 21. The DEM-CFD analyses were conducted using a viscosity that was two-fold lower ($\mu_q = 5.01\ 10^{-4}$ (Pa s)) as compared to the basic one (Table 1).

With falling viscosity, the specimen's compressive strength rose as in the experiment [28]. The strength rise was about 10% (Fig. 21). The lower maximum pore fluid pressure of 0.4 MPa happened for the lower viscosity $\mu_q = 5.01\ 10^{-4}$ (Pa s).

6 Summary and conclusions

This work simulates the behavior of partially fluid-saturation concrete in uniaxial compression under 2D isothermal conditions using an improved fully coupled DEM/CFD-based hydro-mechanical technique. The method takes into account the two-phase laminar flow of fluid in the flow network of predefined channels and discretizes the geometry of pores/cracks with accuracy. The method demonstrated its capacity to evaluate concrete's compressive strength and fracture, and pore fluid pressures of wet concrete specimens. The impacts

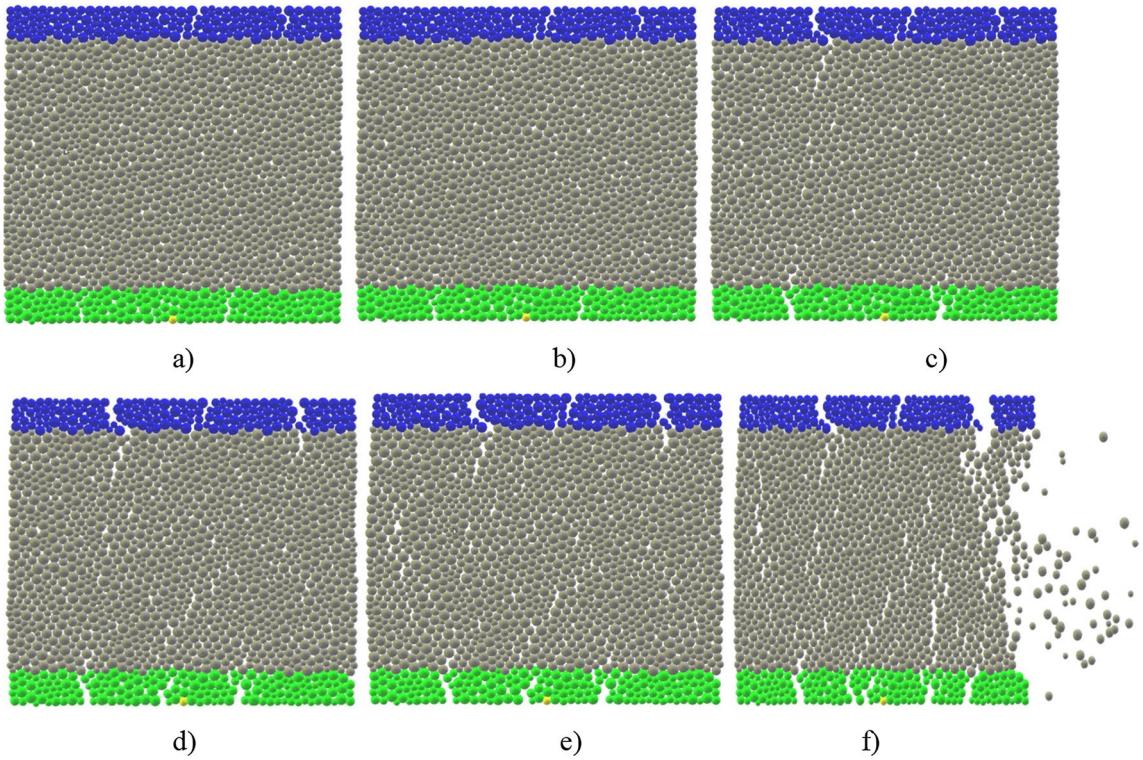

Fig. 12 DEM-CFD simulation results for one-phase partially fluid-saturated concrete specimen ($\alpha_q = 0.7$) during uniaxial compression: evolution of fracture pattern **a** $\varepsilon_y = 0.12\%$, **b** $\varepsilon_y = 0.15\%$, **c** $\varepsilon_y = 0.18\%$, **d** $\varepsilon_y = 0.19\%$, **e** at peak stress ($\varepsilon_y = 0.215\%$) and **f** slightly after peak stress (displacements are magnified by factor 30)

of both fluid saturation and fluid viscosity on the concrete strength and fracture process, and pore fluid pressures were studied, which proved to be significant. The numerical results showed qualitative agreement with laboratory tests in the literature regarding strength reduction with increasing fluid saturation and decreasing viscosity. The 2D simulations for concrete specimens with initial porosity of 5% lead to the following conclusions:

- The compressive strength of concrete for fully fluid-saturated specimens was lower by 15% as compared to dry ones. It decreased with higher fluid saturation. The reduction was almost linear with increasing fluid saturation. The compressive strength of concrete for fully fluid-saturated specimens also dropped by 10% when dynamic fluid viscosity was two-fold higher.
- The material behavior depended on the pore fluid pressure's increase in pores over the initial one caused by initial specimen compaction induced by the compressive load. The pore fluid pressures promoted a fracture process during fluid migration through pores and cracks (higher contact forces occurred) that decreased the compressive strength. The higher the pore fluid pressure, the higher the compressive strength reduction and fluid migration rate.
- Viscous fluid flow in pores and cracks had a higher influence on the quasi-static compressive strength than the pore volume changes themselves.
- In the specimen, the effect of pore fluid pressure in uniaxial compression was the greatest during the initial specimen compaction phase when no micro-cracks were forming. Later, when cracks occurred, the average pore fluid pressures approached a constant value, and the maximum ones decreased and approached next a constant value.

Appendix A

The DEM equations are listed below:

$$\vec{F}_n = K_n U \vec{N}, \tag{A1}$$

$$\vec{F}_s = \vec{F}_{s,prev} + K_s \Delta \vec{X}_s, \tag{A2}$$

$$K_n = E_c \frac{2R_A R_B}{R_A + R_B} \text{ and } K_s = v_c E_c \frac{2R_A R_B}{R_A + R_B}, \tag{A3}$$

$$\vec{F}_s - F^s_{max} - \vec{F}_n \times \tan\mu_c \leq 0 \text{ (before contact breakage)}, \tag{A4}$$

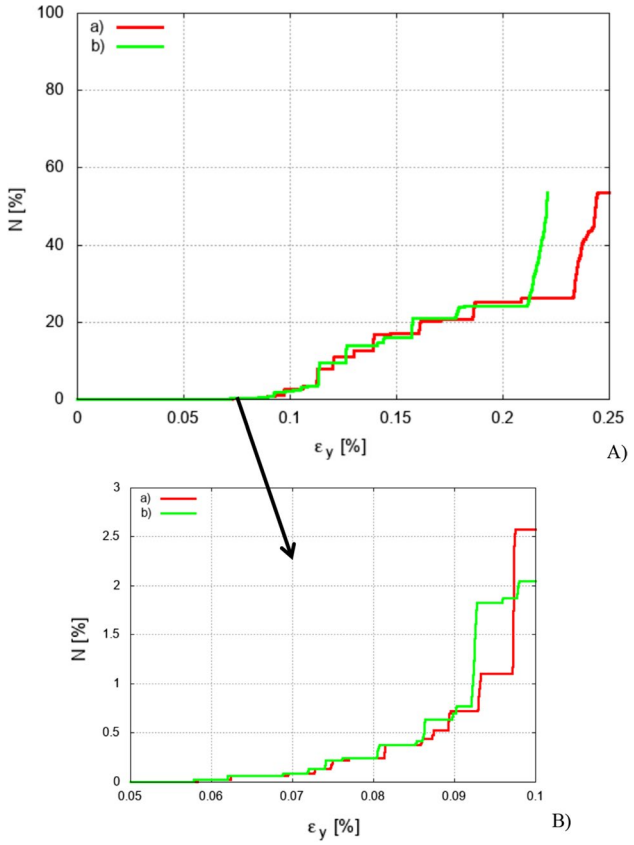

Fig. 13 Pure DEM (curve'a') and DEM-CFD simulation result for one-phase partially fluid-saturated concrete specimen with $\alpha_q = 0.7$ (curve 'b') during uniaxial compression: **A** evolution of relative number N of broken contacts with vertical normal strain ε_y and **B** zoom on onset of contact breakage

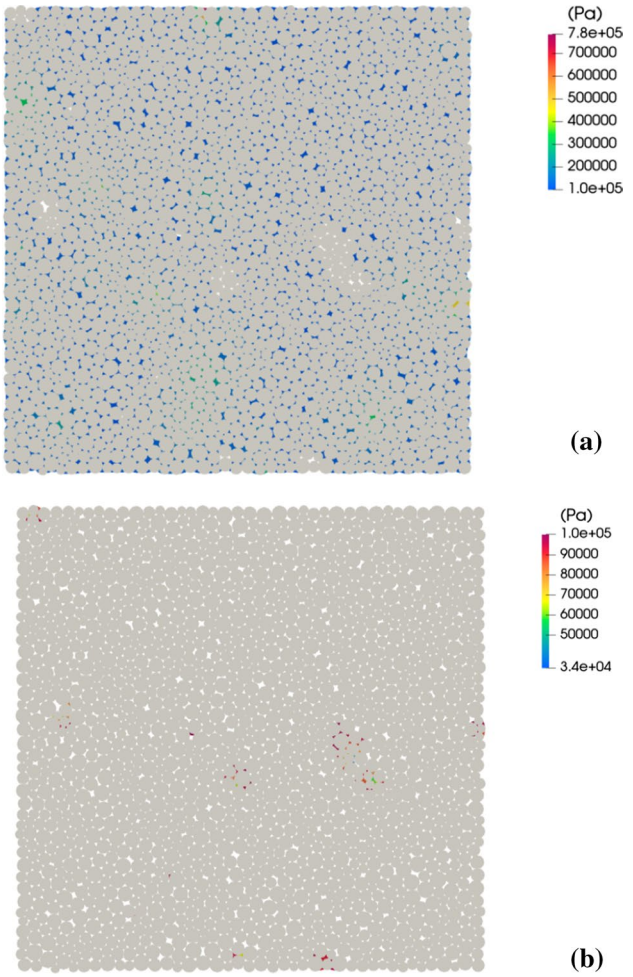

Fig. 14 DEM-CFD results for fully fluid-saturated specimen ($\alpha_q = 1.0$): distribution of high **a** and low **b** pore fluid pressures in concrete specimen for vertical strain $\varepsilon_y = 0.05\%$

$$\vec{F}_s - \vec{F}_n \times \tan\mu_c \leq 0 \text{ (after contact breakage)}, \tag{A5}$$

$$F^s_{max} = CR^2 \text{ and } F^n_{min} = TR^2, \tag{A6}$$

$$\vec{F}^k_{damp} = \vec{F}^k - \alpha_d \cdot \mathrm{sgn}\left(\vec{v}^k_p\right)\vec{F}^k. \tag{A7}$$

where $\vec{F}_n$—the normal contact force, U—the overlap between discrete elements, $\vec{N}$—the unit normal vector at the contact point, $\vec{F}_s$—the tangential contact force, $\vec{F}_{s,prev}$—the tangential contact force in the previous iteration, $\vec{X}_s$—the relative tangential displacement increment, K_n—the normal contact stiffness, K_s—the tangential contact stiffness, E_c—the elastic modulus of the particle contact, υ_c—the Poisson's ratio of particle contact, R—the particle radius, R_A and R_B contacting particle radii, μ_c—the Coulomb inter-particle friction angle, F^s_{max}—the critical cohesive contact force, F^n_{min}—the minimum tensile force, C—the cohesion at the contact (maximum shear stress at zero pressure), and T—the tensile strength of the contact, $\vec{F}^k_{damp}$—the dampened contact force, $\vec{F}^k$ and $\vec{v}^k_p$-kth—the components of the residual force and translational particle velocity v_p and α_d—the positive damping coefficient smaller than 1 (sgn(·) that returns the sign of the kth component of velocity).

Appendix B

The hydraulic aperture h of the artificial channels 'S2S' is computed by a modified empirical formula developed by Hökmark et al. [85]:

$$h = \beta\left(h_{inf} + \left(h_0 - h_{inf}\right)e^{-1.5\cdot 10^{-7}\sigma_n}\right), \tag{B1}$$

where h_{inf}—the hydraulic aperture for the infinite normal stress, h_0—the hydraulic aperture for the zero normal stress,

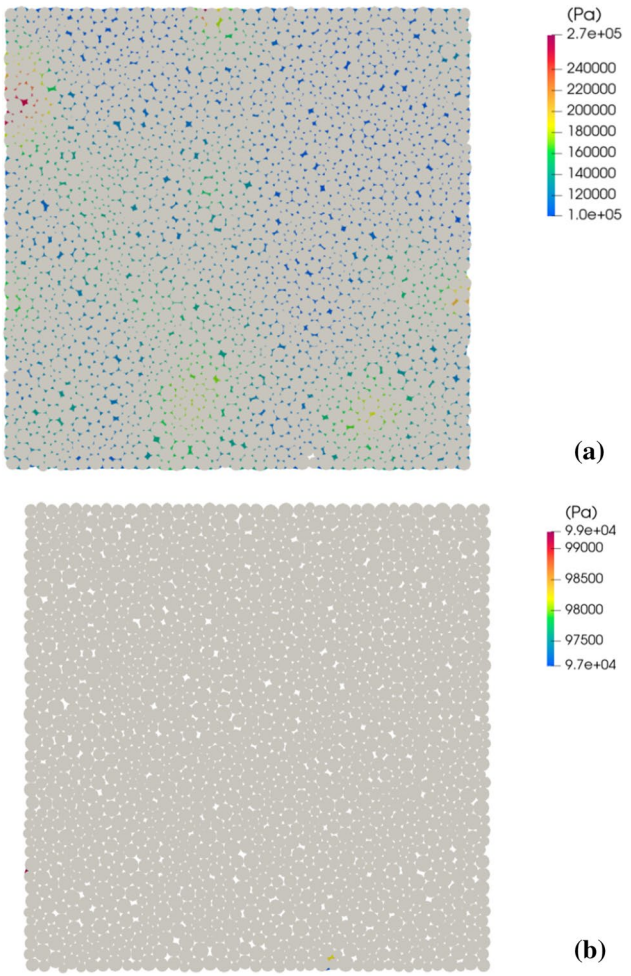

Fig. 15 DEM-CFD results for fully fluid-saturated specimen ($\alpha_q = 1.0$): distribution of high **a** and low **b** pore fluid pressures in concrete specimen for vertical strain $\varepsilon_y = 0.10\%$

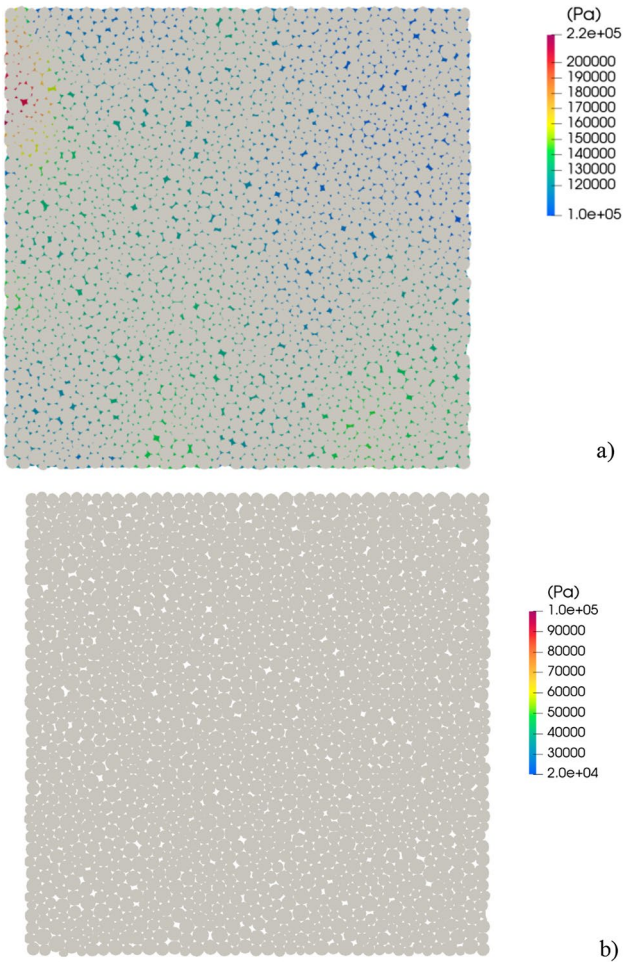

Fig. 16 DEM-CFD results for fully fluid-saturated specimen ($\alpha_q = 1.0$): distribution of high **a** and low **b** pore fluid pressures in concrete specimen for vertical strain $\varepsilon_y = 0.19\%$ (peak stress)

σ_n—the effective normal stress at the particle contact and β—the aperture coefficient. The geometry of the nearby triangles has a direct bearing on the hydraulic aperture of the actual channels 'T2T' (Fig. 22) as

$$h = \gamma e \cos(90° - \omega), \tag{B2}$$

where e is the edge length between two adjacent triangles, ω denotes the angle between the edge with the length e and the center line of the channel that connects two adjacent triangles, and γ is the reduction factor established to maintain the maximum Reynolds number Re along the main flow route at a value below the critical value for laminar flow ($Re = 2100$). The parameter γ was determined in parametric tests at fluid pressure up to 140 MPa.

Following Barmak et al. [86], the continuity and momentum equations are developed that are rendered dimensionless

$$div\,\mathrm{u}_j = 0, \tag{B3}$$

$$\frac{\partial \mathrm{u}_j}{\partial t} + (\mathrm{u}_j \cdot \nabla)\mathrm{u}_j = -\frac{\rho_q}{r\rho_j}\nabla p_j + \frac{1}{\mathrm{Re}_p}\frac{\rho_q}{r\rho_j}\frac{m\mu_j}{\mu_q} \cdot \mathrm{u}_j, \tag{B4}$$

where $\mathrm{u}_j = (u_j, v_j)$ and p_j are the velocity and pressure of the fluid phase j, ρ_j and μ_j are the corresponding density and dynamic viscosity. The Reynolds number is $\mathrm{Re}_p = \rho_p u_i h_p/\mu_p$ and the density and viscosity ratios are $r = \rho_q/\rho_p$ and $m = \mu_q/\mu_p$. The lower and upper phases in the dimensionless formulation, are located in the regions $-n_d \le y \le 0$ and $0 \le y \le 1$, where $n_d = h_q/h_p$. The velocities satisfy the no-slip boundary condition at the channel walls.

$$\mathrm{u}_q(y = -n_d) = 0 \text{ and } \mathrm{u}_p(y = 1) = 0. \tag{B5}$$

The continuity of velocities and tangential stresses is required by the boundary conditions at the interface at $y = 0$ [86]

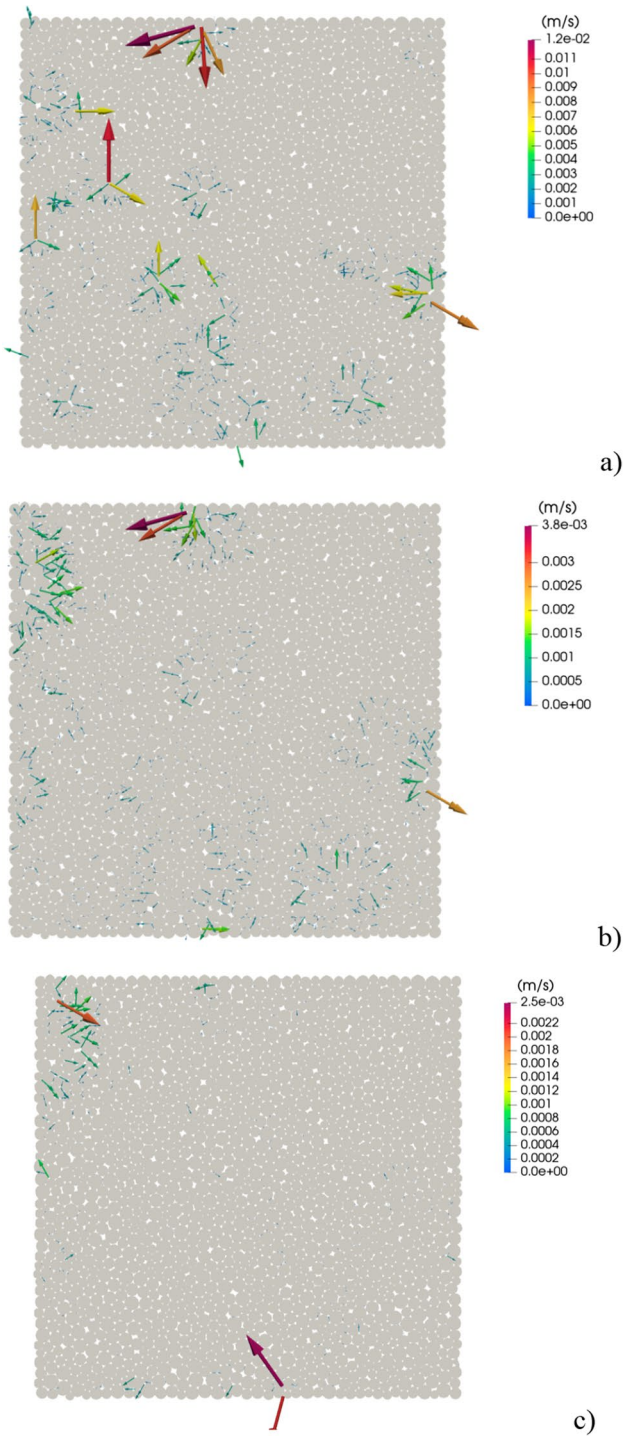

Fig. 17 DEM-CFD results for fully fluid-saturated specimen ($\alpha_q = 1.0$): distribution of fluid velocity vectors specimen for vertical normal strain ε_y: **a** $\varepsilon_y = 0.05\%$, **b** $\varepsilon_y = 0.10\%$ and **c** $\varepsilon_y = 0.19\%$ (peak stress)

$$u_q(y=0) = u_p(y=0) \tag{B6}$$

and

$$\mu_q \left.\frac{\partial u_q}{\partial y}\right|_{y=0} = \mu_p \left.\frac{\partial u_p}{\partial y}\right|_{y=0}. \tag{B7}$$

The mass flow rates $M_{q,x}$ and $M_{p,x}$ for both fluid phases are derived by solving Eqs. B3 and B4 with the boundary conditions (Eqs. B5–B7), as well as the shear stress τ_{f0} at the channel surfaces.

The fluid in VPs (triangular cells), in contrast to the model of fluid flow in the channels, is presumed to be compressible. The discretized form of the mass conservation equation for the liquid phase is

$$\frac{\alpha_{q,i}^{n+1}\rho_{q,i}^{n+1}V_i^{n+1} - \alpha_{q,i}^{n}\rho_{q,i}^{n}V_i^{n}}{\Delta t} + \sum_f \left(\rho_{q,f}^{n} U_f^{n} \alpha_{q,f}^{n}\right) = 0 \tag{B8}$$

with

$$V_i^{n+1} = V_i^{n} + \frac{\mathrm{d}V}{\mathrm{d}t}\Delta t, \tag{B9}$$

where V_i^{n+1} and V_i^{n} are the volume of VP_i at a time increment $n+1$ and n (the third dimension is the unit dimension), respectively, f is the face (edge) number, U_f^n denotes the volume flux through the face (m^3/s), based on the average velocity in the channel, $\alpha_{q,f}^n$ is the face value of the liquid phase volume fraction (–), t is the time step (s), n denotes the time increment and i is the VP number (–). The same equations are defined for the gas phase.

VPs in contrast to the channel flow model assume that the fluid is compressible. The mass flow rates of fluid phases in channels are only calculated to estimate the mass flow rate of fluid flowing through the cell faces. The fluid pressure can exceed 70 MPa in specific situations, such as during the hydraulic fracturing process. The gas phase exceeds the critical point and becomes a supercritical fluid under these conditions. Therefore, for both fluid phases in VPs, the Peng-Robinson equation of state [69] is used to describe fluid behavior above the critical point

$$P = \frac{RT}{\left(V_{q/p} - b_{q/p}\right)} - \frac{a_{q/p}}{\left(V_{q/p}^2 + 2b_{q/p}V_q - b_{q/p}^2\right)}, \tag{B10}$$

where P is the pressure (Pa), R denotes the gas constant ($R = 8314{,}4598$ J/(kmol K)), $V_{q/p}$ is the molar volume of liquid (q) and gas (p) fraction (m^3/kmol) and T denotes the temperature (K). The parameters in Eq. B10 are:

$$a_{q/p}(T) = a_{q/p,0}\left[1 + n_{q/p}\left(1 - \left(\frac{T_i^n}{T_{q/p,c}}\right)^{0.5}\right)\right]^2, \tag{B11}$$

$$n_{q/p} = 0.37464 + 1.54226\omega_{q/p} - 0.26992\omega_{q/p}^2, \tag{B12}$$

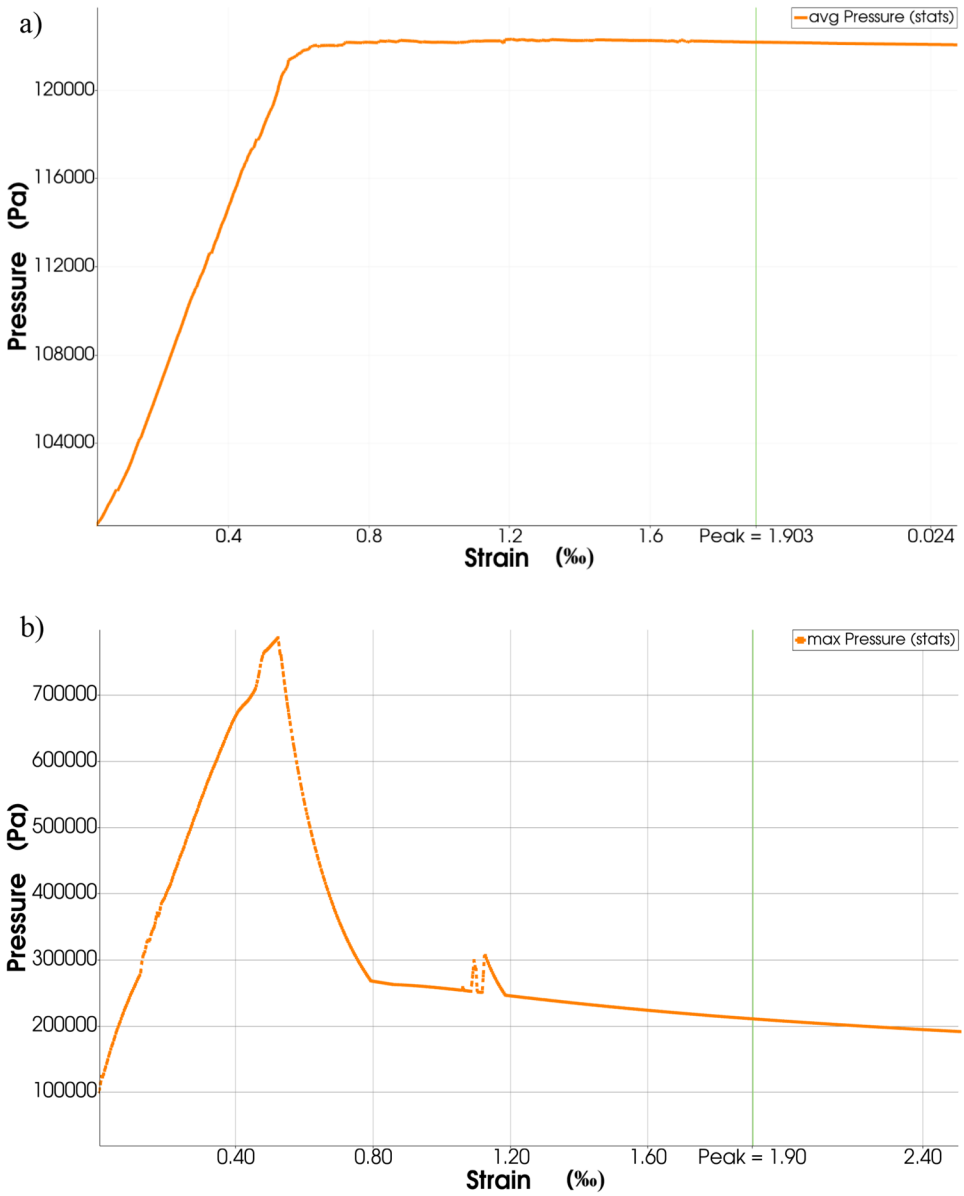

Fig. 18 DEM-CFD results for fully fluid-saturated specimen (with $\alpha_q = 1.0$): evolution of average **a** and maximum pore fluid pressure **b** against vertical normal strain ε_y during uniaxial compression

$$a_{q/p,0} = a_{c,q/p}\beta(T), \tag{B13}$$

$$a_{c,q/p} = \frac{0.457247R^2T^2_{q/p,c}}{P_{q/p,c}}, \tag{B14}$$

$$b_{q/p} = \frac{0.07780RT_{q/p,c}}{P_{q/p,c}}, \tag{B15}$$

$$\beta = \left[1 + c_1\left(1 - T_r^{\frac{1}{2}}\right) + c_2\left(1 - T_r^{\frac{1}{2}}\right)^2 + c_3\left(1 - T_r^{\frac{1}{2}}\right)^3\right]^2, \tag{B16}$$

where $T_{q/p,c}$ is the critical temperature of phase (K), $P_{q/p,c}$ denotes the critical pressure of phase (Pa), $\omega_{q/p}$ is the acentric factor of phase (–), and T_r denotes the reduced temperature $\frac{T}{T_c}$. When $c_1 = c_2 = c_3 = 0$, the original model is obtained. The extra factors help connect vapor pressure data from highly polar liquids like water and methanol. For most substances, Equations B11–B16 provide a good fit for the vapor pressure, however predicting molar volumes for liquid phase can be very inaccurate. The forecast of saturated liquid molar quantities might deviate by l0–40% [87]. Peneloux and Rauzy [88] proposed an effective correction term

$$V_q^{corr} = V_q + s, \tag{B17}$$

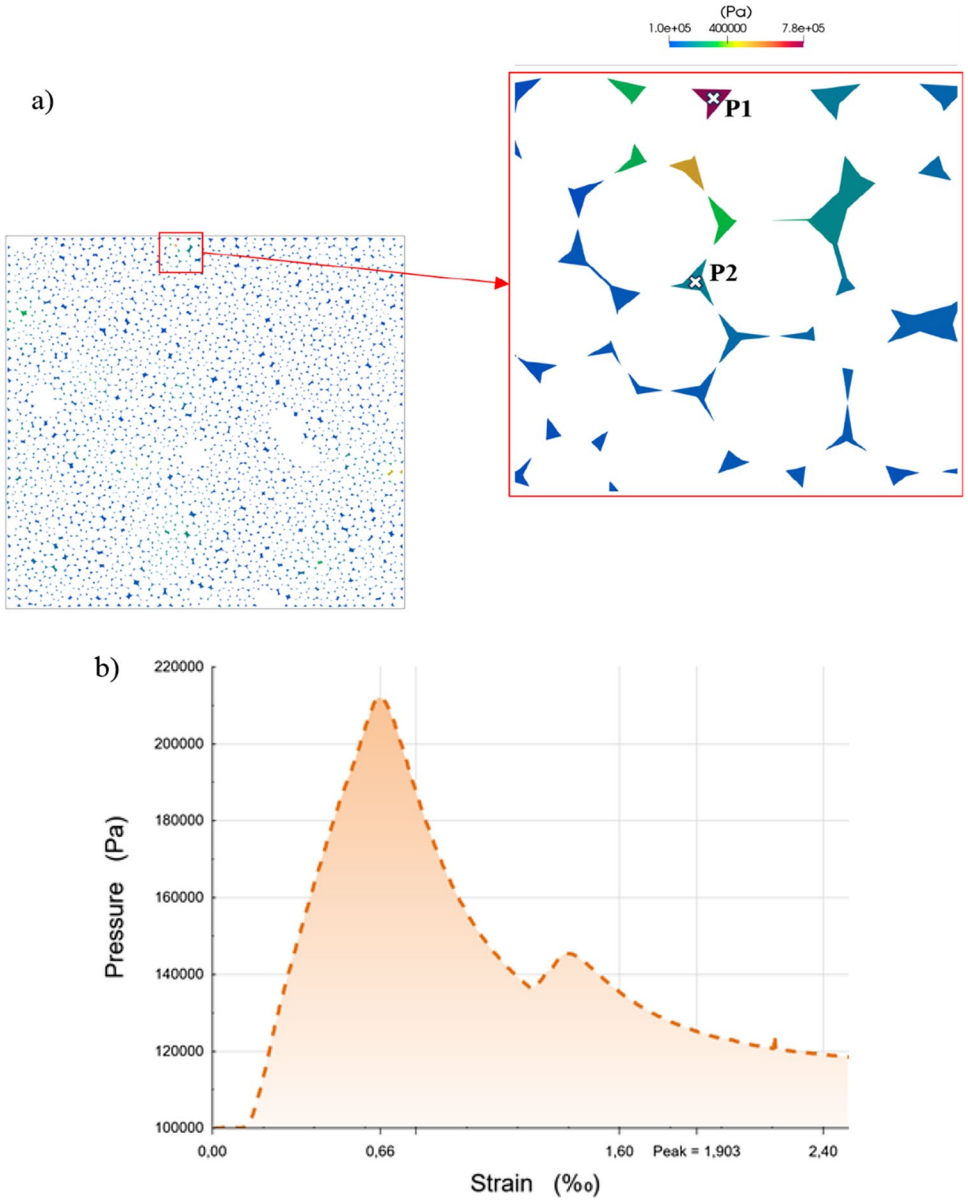

Fig. 19 DEM-CFD results for fully fluid-saturated specimen ($\alpha_q = 1.0$): evolution of pore fluid pressure in vicinity of maximum fluid pressure (point 'P1') against vertical normal strain ε_y: **a** location of measurement points '1' and '2', and **b** evolution of fluid pressure in point 'P2' in vicinity of point 'P1'

where s is the small molar volume correction term that is component dependent; V_q is the molar volume predicted by Eq. B16 and V_q^{corr} refers to the corrected molar volume. The value of s is negative for higher molecular weight non-polar and essentially for all polar substances. The molar volume correction term is considered to be 0.0 m^3/kmol and − 0.0034 m^3/kmol for the gas phase and liquid phase (water), respectively. The Peng-Robinson equation of state has the advantage of being able to describe the behavior of supercritical fluids at extremely high fluid pressures and temperatures. For each phase, the mass conservation equation is used. The mass transfer between phases and the grid velocity is ignored when there is no internal mass source. The discretized form of the mass conservation equation for the liquid phase is

$$\frac{\alpha_{q,i}^{n+1}\rho_{q,i}^{n+1}V_i^{n+1} - \alpha_{q,i}^{n}\rho_{q,i}^{n}V_i^{n}}{\Delta t} + \sum_f \left(\rho_{q,f}^{n} U_f^{n} \alpha_{q,f}^{n}\right) = 0 \qquad \text{(B18)}$$

with

$$V_i^{n+1} = V_i^{n} + \frac{dV}{dt}\Delta t, \qquad \text{(B19)}$$

where f is the face (edge) number, U_f^n denotes the volume flux through the face (m^3/s), based on the average velocity in the channel, $\alpha_{q,f}^n$ is the face value of the fluid phase volume fraction (–), t is the time step (s), n denotes the time increment and i is the VP number (–). The explicit formulation is used instead of an iterative solution of the transport equation during each time step since the volume fraction at the

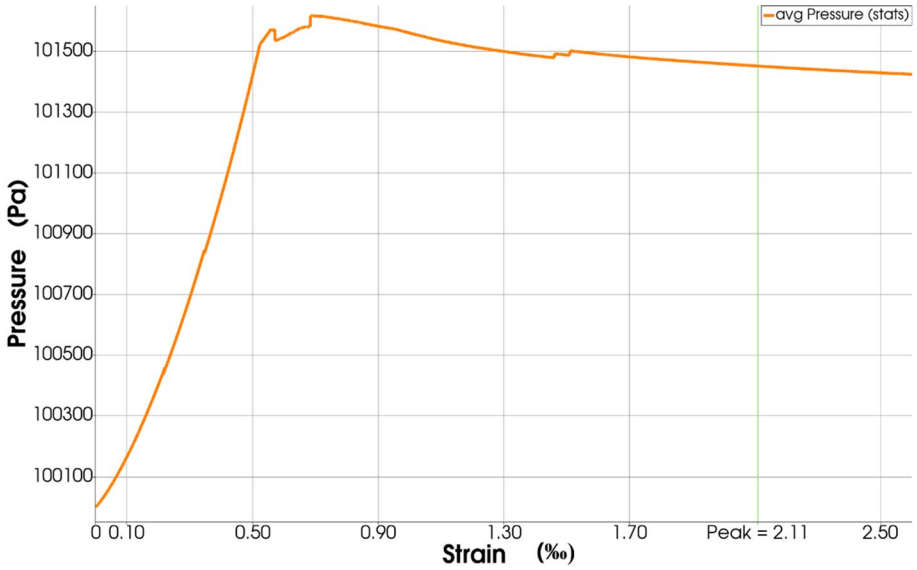

Fig. 20 DEM-CFD results for partially fluid-saturated concrete specimen (with $\alpha_q = 0.7$): evolution of average pore fluid pressure against vertical normal strain ε_y during uniaxial compression

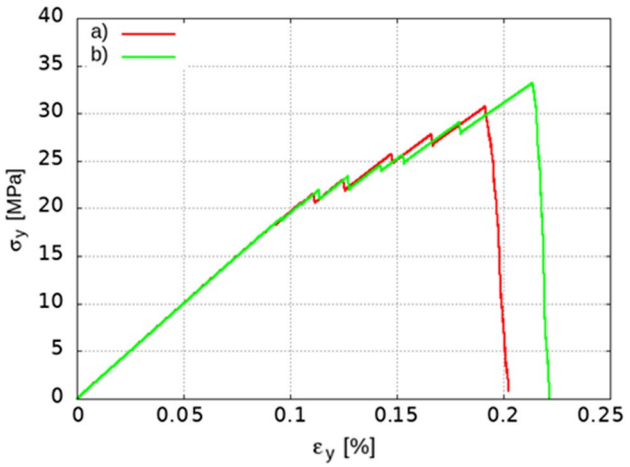

Fig. 21 DEM-CFD simulation results for one-phase fully saturated concrete specimen ($\alpha_q = 1.0$) during uniaxial compression with fluid dynamic viscosity μ_q: relationship between vertical normal stress σ_y and vertical normal strain ε_y for two different fluid viscosities: **a** $\mu_q = 10.02\ 10^{-4}$ Pa s and **b** $\mu_q = 5.01\ 10^{-4}$ Pa s

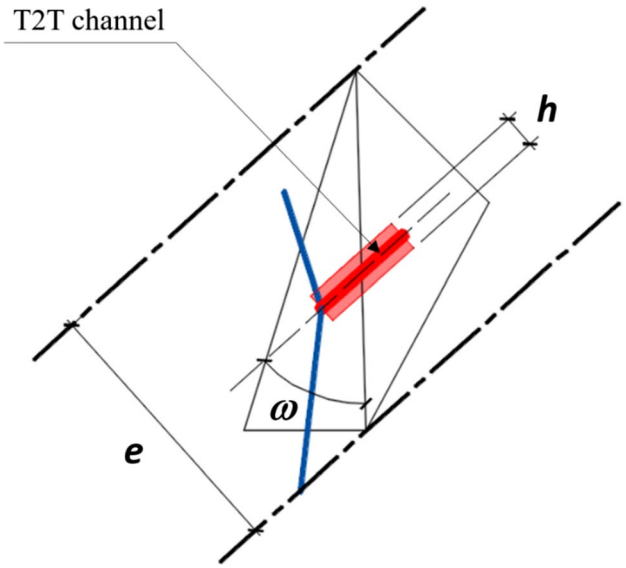

Fig. 22 'T2T' channel (red colour denotes channel width h) (colour figure online)

current time step is directly computed from known quantities at the previous time step. Similarly, the mass conservation equation for a gas phase is introduced. The product $\rho_q U_f^n \alpha_{q,f}^n$ in Eq. B18 is the mass flow rate $M_{q,f}$ of the liquid phase flowing through the face f (edge of a triangle) of VP_i. The density of the liquid phase can be calculated by solving the mass conservation equation for both phases

$$\rho_{i,q}^{n+1} = \frac{\alpha_{q,i}^n \rho_{q,i}^n V_i^n + \Delta t \sum_f M_{q,f}}{\left(V_i^n + \Delta V_i \Delta t\right) \alpha_{q,i}^{n+1}}. \tag{B20}$$

The density of the gas phase can also be computed in the same way. It should be noted that the molar volume V (q/p) is related to the gas density.

$$V_{i,p}^{n+1} = \frac{w_p}{\rho_{i,p}^{n+1}}, \tag{B21}$$

and to the liquid density

$$V_{i,q}^{n+1} = \frac{w_q}{\rho_{i,q}^{n+1}} - s. \tag{B22}$$

where w_p and w_q are molar weights of gas and liquid phases, respectively. Due to the fact that the fluid phases share the same pressure

$$\frac{RT_i^n}{\left(V_{i,p}^{n+1} - b_p\right)} - \frac{a_p}{\left(V_{i,p}^{n+12} + 2b_p V_{i,p}^{n+1} - b_p^2\right)} = \frac{RT_i^n}{\left(V_{i,q}^{n+1} - b_q\right)} - \frac{a_q}{\left(V_{i,q}^{n+12} + 2b_q V_{i,q}^{n+1} - b_q^2\right)}, \tag{B23}$$

the fluid phase fractions are computed. Inserting Eq. B21 for the gas phase and Eq. B22 for the liquid phase into Eq. B23, a polynomial equation is obtained with respect to the liquid fraction $\alpha_{q,i}^{n+1}$. The gas-phase fraction is computed as $\alpha_{p,i}^{n+1} = 1 - \alpha_{q,i}^{n+1}$. Equation B10 is used to calculate the new pressure P_i^{n+1} in $\mathrm{VP_i}$. The explicit formulation is utilized instead of an iterative solution of the transport equation during each time step.

Because of the passage of a viscous fluid, there is shear stress along the channel's edge. The shear stress profile in the fluid is triangular for immovable parallel plates with no-slip boundary conditions (zero velocity). The shear stress τ_{f0} at the interface between liquid and gas is

$$\tau_{f0} = \frac{h}{2}\frac{P_i^n - P_j^n}{L}. \tag{B25}$$

The fluid pressures in VPs and 'S2S' channels are converted into the forces $\vec{F}_{P,j}$ and $\vec{F}_{S,j}$ acting on spheres. For simplicity, the fluid pressure forces acting on the sphere are calculated by assuming that the fluid–solid contact area is multiplied by the pressure in the cell ($\vec{F}_{P,j}$) or channel ($\vec{F}_{S,j}$). The contact area is calculated as a section of the cylinder's surface with a height equal to the diameter of the sphere, and not as a section of the sphere's surface. This simplifies the computational algorithm and only slightly overestimates the forces

$$\vec{F}_{P,j} = -P_i \vec{n} A_k, \tag{B26}$$

where $\vec{n}$—the unit vector normal to the discretized sphere's edge, P_i—the pressure in VP, i—the VP number, j—the sphere number, and A_k—the contact area between the fluid in VP_i and sphere

$$A_k = 2r_j e_k, \tag{B27}$$

with r_j—the sphere radius and e_k—the sphere edge length. The shear stresses are finally converted into the forces acting on spheres as

$$\vec{F}_{S,j} = \tau_{f0,i}\vec{I}A_k \text{ with } A_k = 2r_j L_k, \tag{B28}$$

where $\vec{I}$—the unit vector parallel to the channel wall and oriented in the fluid flow direction, $\tau_{f0,i}$—the shear stress in the channel, i—the channel number, j—the sphere number and A_k—the contact area between the channel and sphere, and L_k—the channel length.

Acknowledgements The present study was supported by the research project "*Fracture propagation in rocks during hydro-fracking-experiments and discrete element method coupled with fluid flow and heat transport*" (years 2019–2023), and financed by the National Science Centre (NCN) (UMO-2018/29/B/ST8/00255).

Author contributions MK: Conceptualization, Methodology, Investigation, Writing— original draft, Writing—review & editing, JT: Conceptualization, Methodology, Writing—original draft, Writing—review & editing, MN: Investigation.

Data availability Data will be made available on request.

Declarations

Conflict of interest The authors declare that they have no known competing financial interests or personal relationships that could have appeared to influence the work reported in this paper.

References

1. Rossi, P., Boulay, C.: Influence of free water in concrete on the cracking process. Mag. Concr. Res. **1990**(42), 143–146 (1990)
2. Rossi, P.: Influence of cracking in presence of free water on the mechanical behavior of concrete. Mag. Concr. Res. **43**, 53–57 (1991)
3. Li, G.: The effect of moisture content on the tensile strength properties of concrete. University of Florida, Gainesville, FL, USA (2004)
4. Wittmann, F.H., Sun, Z., Zhao, T.: Strength and fracture energy of concrete in seawater. In Proceedings of the 6th International Conference on Fracture Mechanics of Concrete and Concrete Structures, Catania, Italy, 17–22 June (2007)
5. Wang, H.L., Li, Q.B.: Experiments on saturated concrete under dfferent splitting tensile rate and mechanism on strength change. Eng. Mech. **24**, 105–109 (2007)
6. Yan, D.M., Lin, G., Wang, Z.: Research on dynamic direct tensile properties of concrete under different environments. J. Dalian Univ. Technol. **45**, 416–421 (2005)
7. Deng, H.F., Yuan, X.F., Li, J.L.: Fracture mechanics characteristics and deterioration mechanism of sandstone under reservoir immersion interaction. J. Earth Sci. China Univ. Geosci. **39**, 108–114 (2014)
8. Zhang, P., Sun, Z.W., Zhao, T.J.: Fracture energy and strain softening of concrete under seawater environment. J. Civ. Arch. Environ. Eng. **32**, 72–77 (2010)
9. Reinhardt, H.W., Rossi, P., van Mier, J.G.M.: Joint investigation of concrete at high rates of loading. Mater. Struct. **23**, 213–216 (1990)
10. Ross, C., Jerome, D.M., Tedesco, J.E.: Moisture and strain rate effects on concrete strength. ACI Mater. J. **93**, 293–300 (1996)

11. Wang, J., Sun, K., Hu, Y., Guan, Q., Li, Q.: The mechanical properties of concrete in water environment: a review. Front. Mater. **9**, 996650 (2022)
12. Shen, J., Xu, Q.: Effect of moisture content and porosity on compressive strength of concrete during drying at 105 °C. Constr. Build. Mater. **195**, 19–27 (2019)
13. Zhang, G., Li, X., Li, Z.: Experimental study on static mechanical properties and moisture contents of concrete under water environment. Sustainability **11**, 2962 (2019)
14. Yousheng, D., Weiling, Y.: Research progress on the effect of environmental water on the static strength of concrete. Adv. Sci. Technol. Water Resour. **35**(4), 99–103 (2015)
15. Malecot, Y., Zingg, L., Briffaut, M., Baroth, J.: Influence of free water on concrete triaxial behavior: the effect of porosity. Cem. Concr. Res. **120**, 207–216 (2019)
16. Piotrowska, E., Forquin, P.: Experimental investigation of the confined behavior of dry and wet high-strength concrete: quasi static versus dynamic loading. J. Dyn. Behav. Mater. **1**(2), 191–200 (2015)
17. Vu, X.H., Malecot, Y., Daudeville, L., Buzaud, E.: Experimental analysis of concrete behavior under high confinement: effect of the saturation ratio. Int. J. Solids Struct. **46**(5), 1105–1120 (2009)
18. Boxu, M., Jinyu, X., Chuanxin, L., Chao, G., Guang, P.: Effect of water content on tensile properties of cement mortar. IOP Conf. Ser.: Earth Environ. Sci. **189**, 032023 (2018)
19. Chen, X., Huang, W., Zhou, J.: Effect of moisture content on compressive and split tensile strength of concrete. Indian J. Eng. Mater. Sci. **19**, 427–435 (2012)
20. Zhu, F.Z., Liu, J., Li, Z.L.: Discussion on the influence of water content in concrete dynamic elastic modulus test. J. Concr. **11**, 40–41 (2012)
21. Shoukry, S.N., William, G.W., Riad, M.Y., Downie, B. Effect of moisture and temperature on the mechanical properties of concrete. Proceedings of the SEM Annual Conference June 1–4, 2009 Albuquerque New Mexico USA, (2009)
22. Cadoni, E., Labibes, K., Albertini, C.: Strain-rate effect on the tensile behavior of concrete at different relative humidity levels. Mater. Struct. **34**, 21–26 (2001)
23. Wang, H.L., Li, Q.B.: Experiments of the compressive properties of dry and saturated concrete under different loading rates. J. Hydroelectr. Eng. **26**, 84–89 (2007)
24. Fu, Q., Zhang, Z., Zhao, X., Hong, M., Guo, B., Yuan, Q., Niu, D.: Water saturation effect on the dynamic mechanical behaviour and scaling law effect on the dynamic strength of coral aggregate concrete. Cement Concr. Compos. **120**, 104034 (2021)
25. Xu, W.B., Li, Q.B., Hu, Y.: Water content variations in the process of concrete setting. J. Hydroelectr. Eng. **36**(07), 92–103 (2017)
26. Oshita, H., Tanabe, T.: Water migration phenomenon model in cracked concrete I: formulation. J. Eng. Mech. **126**, 539–543 (2000)
27. Wang, H.L., Li, Q.B., Sun, X.Y., Jin, W.L.: Mesomechanism of tensile strength reduction and tension constitutive model of saturated concrete. J. Basic Sci. Eng. **16**, 65–72 (2008)
28. Zhang, X., Chiu, Y., Hong Hao, H., Cui, J.: Free water effect on the dynamic compressive properties of mortar. Cement Concr. Compos. **118**, 103933 (2021)
29. Weiss, T., Siegesmund, S., Kirchner, D., Sippel, J.: Insolation weathering and hygric dilatation: two competitive factors in stone degradation. Environ. Geol. **46**, 402–413 (2004)
30. Sun, X., Wang, H., Cheng, X., Sheng, Y.: Effect of pore liquid viscosity on the dynamic compressive properties of concrete. Constr. Build. Mater. **231**, 117143 (2020)
31. Krzaczek, M., Kozicki, J., Nitka, M., Tejchman, J.: Simulations of hydro-fracking in rock mass at meso-scale using fully coupled DEM/CFD approach. Acta Geotech. **15**, 297–324 (2020)
32. Krzaczek, M., Nitka, M., Tejchman, J.: Effect of gas content in macropores on hydraulic fracturing in rocks using a fully coupled DEM/CFD approach. Int. J. Numer. Anal. Meth. Geomech. **45**(2), 234–264 (2021)
33. Bolander, J.E., Eliáš, J., Cusatis, G., Nagai, K.: Discrete mechanical models of concrete fracture. Eng. Fract. Mech. **257**, 108030 (2021)
34. Skarżyński, L., Nitka, M., Tejchman, J.: Modelling of concrete fracture at aggregate level using FEM and DEM based on x-ray μCT images of internal structure. Eng. Fract. Mech. **10**(147), 13–35 (2015)
35. Nitka, M., Tejchman, J.: Modelling of concrete behaviour in uniaxial compression and tension with DEM. Granular Matter **217**(1), 145–164 (2015)
36. Nitka, M., Tejchman, J.: A three-dimensional meso scale approach to concrete fracture based on combined DEM with X-ray μCT images. Cem. Concr. Res. **107**, 11–29 (2018)
37. Suchorzewski, J., Tejchman, J., Nitka, M.: Discrete element method simulations of fracture in concrete under uniaxial compression based on its real internal structure. Int. J. Damage Mech **27**(4), 578–607 (2014)
38. Suchorzewski, J., Tejchman, J., Nitka, M.: Experimental and numerical investigations of concrete behaviour at meso-level during quasi-static splitting tension. Theoret. Appl. Fract. Mech. **96**, 720–739 (2018)
39. Singh, K., Menke, H., Andrew, M., et al.: Dynamics of snap-off and pore-filling events during two-phase fluid flow in permeable media. Sci. Rep. **7**, 5192 (2017)
40. Shams, M., Singh, K., Bijeljic, B., Blunt, M.J.: Direct numerical simulation of pore-scale trapping events during capillary-dominated two-phase flow in porous media. Transp Porous Med **138**, 443–458 (2021)
41. Krzaczek, M., Nitka, M., Tejchman, J.: Modelling hydraulic and capillary-driven two-phase fluid flow in unsaturated concretes at the meso-scale with a unique coupled DEM-CFD technique. Int J Numer Anal Methods Geomech. **47**(1), 23–53 (2023)
42. Cundall, P.: Fluid formulation for PFC2D. Itasca Consulting Group, Minneapolis, Minnesota (2000)
43. Hazzard, J.F., Young, R.P., Oates, J.S.: Numerical modeling of seismicity induced by fluid injection in a fractured reservoir. Proceedings of the 5th North American Rock Mechanics Symposium, Miningand Tunnel Innovation and Opportunity, Toronto, Canada, 7–10 July 2002, pp. 1023–1030 (2002)
44. Al-Busaidi, A., Hazzard, J.F., Young, R.P.: Distinct element modeling of hydraulically fractured distinct element modeling of hydraulically fractured lac du bonnet granite. J. Geophys. Res. **110**, 06302 (2005)
45. Yoon, J.S., Zang, A., Stephansson, O.: Numerical investigation on optimized stimulation of intact and naturally fractured deep geothermal reservoirs using hydro-mechanical coupled discrete particles joints model. Geothermic **52**, 165–184 (2014)
46. Shimizu, H., Murata, S., Ishida, T.: The distinct element analysis for hydraulic fracturing in hard rock considering fluid viscosity and particle size distribution. Int J Rock Mech Mining Sci. **48**, 712–727 (2011)
47. Ma, X., Zhou, T., Zou, Y.: Experimental and numerical study of hydraulic fracture geometry in shale formations with complex geologic conditions. J. Struct. Geol. **98**, 53–66 (2017)
48. Liu, G., Sun, W., Lowinger, S.M., Zhang, Z., Huang, M., Peng, J.: Coupled flow network and discrete element modeling of

injected-induced crack propagation and coalescence in brittle rock. Acta Geotech. **14**(3), 843–869 (2019)
49. Zhang, G., Li, M., Gutierrez, M.: Numerical simulation of proppant distribution in hydraulic fractures in horizontal wells. J Nat Gas Sci Eng. **48**, 157–168 (2017)
50. Xiao-Dong, N., Zhu, C., Wang, Y.: Hydro-mechanical analysis of hydraulic fracturing based on an improved DEM-CFD coupling model at micro-level. J. Comput. Theor. Nanosci. **12**(9), 2691–2700 (2015)
51. Zeng, J., Li, H., Zhang, D.: Numerical simulation of proppant transport in hydraulic fracture with the upscaling CFD-DEM method. J Nat Gas Sci Eng. **33**, 264–277 (2016)
52. Zhang, G., Sun, S., Chao, K., et al.: Investigation of the nucleation, propagation and coalescence of hydraulic fractures in glutenite reservoirs using a coupled fluid flow-DEM approach. Powder Technol. **354**, 301–313 (2019)
53. Lathama, J.P., Munjiz, A., Mindel, J., et al.: Modelling of massive particulates for breakwater engineering using coupled FEM/DEM and CFD. Particuology **6**, 572–583 (2008)
54. Chareyre, B., Cortis, A., Catalano, E., Barthélemy, F.: Pore-scale modeling of viscous flow and induced forces in dense sphere packings. Transp. Porous Media **94**(2), 595–615 (2012)
55. Catalano, E., Chareyre, B., Barthélémy, F.: Pore-scale modeling of fluid-particles interaction and emerging poromechanical effects. Int. J. Numer. Anal. Meth. Geomech. **238**, 51–71 (2014)
56. Papachristos, E., Scholtès, L., Donzé, F.V., Chareyre, B.: Intensity and volumetric characterizations of hydraulically driven fractures by hydro-mechanical simulations. Int. J. Rock Mech. Min. Sci. **93**, 163–178 (2017)
57. Caulk, R., Sholtès, L., Krzaczek, M., Chareyre, B.: A pore-scale thermo–hydro-mechanical model for particulate systems. Comput. Methods Appl. Mech. Eng. **372**, 113292 (2020)
58. Bolander, J.E., Berton, S.: Simulation of shrinkage induced cracking in cement composite overlays. Cement Concr. Compos. **26**, 861–871 (2004)
59. Grassl, P., Bolander, J.: Three-dimensional network model for coupling of fracture and mass transport in quasi-brittle geomaterials. Materials **9**, 782 (2016)
60. Luković, M., Šavija, B., Schlangen, E., Ye, G., van Breugel, K.: A 3D lattice modelling study of drying shrinkage damage in concrete repair systems. Materials **9**(2016), 575 (2016)
61. Athanasiadis, I., Wheeler, S.J., Grassl, P.: Hydro-mechanical network modelling of particulate composites. Int. J. Solids Struct. **130–131**(2018), 49–60 (2018)
62. Eliáš, J., Cusatis, G.: Homogenization of discrete mesoscale model of concrete for coupled mass transport and mechanics by asymptotic expansion. J. Mech. Phys. Solids **167**, 105010 (2022)
63. Mašek, J., Květoň, J., Eliáš, J.: Adaptive discretization refinement for discrete models of coupled mechanics and mass transport in concreto. Constr. Build. Mater. **395**, 132243 (2023)
64. Forquin, P., Sallier, L., Pontiroli, C.: A numerical study on the influence of free water content on the ballistic performances of plain concrete targets. Mech. Mater. **89**, 176–189 (2015)
65. Bian, H.B., Jia, Y., Pontiroli, C., Shao, J.F.: Numerical modeling of the elastoplastic damage behavior of dry and saturated concrete targets subjected to rigid projectile penetration. Int. J. Numer. Anal. Meth. Geomech. **42**(2), 312–338 (2018)
66. Benniou, H., Accary, A., Malecot, Y., Briffaut, M., Daudeville, L.: Discrete element modeling of concrete under high stress level: influence of saturation ratio. Comput. Part. Mech. **8**(1), 157–167 (2021)
67. Abdi, R., Krzaczek, M., Tejchman, J.: Comparative study of high-pressure fluid flow in densely packed granules using a 3D CFD model in a continuous medium and a simplified 2D DEM-CFD approach. Granular Matter **24**(1), 1–25 (2022)
68. Abdi, R., Krzaczek, M., Tejchman, J.: Simulations of high-pressure fluid flow in a pre-cracked rock specimen composed of densely packed bonded spheres using a 3D CFD model and simplified 2D coupled CFD-DEM approach. Powder Technol. **417**, 118238 (2023)
69. Krzaczek, M., Nitka, M., Tejchman, J.: A novel DEM-based pore-scale thermal-hydro-mechanical model for fractured non-saturated porous materials. Acta Geotech. **18**, 2487–2512 (2023)
70. Krzaczek, M., Tejchman, J.: Hydraulic fracturing process in rocks – small-scale simulations with a novel fully coupled DEM/CFD-based thermo-hydro-mechanical approach. Eng. Fract. Mech. **289**, 109424 (2023)
71. Kozicki, J., Donze, F.V.: A new open-source software developer for numerical simulations using discrete modeling methods. Comput. Methods Appl. Mech. Eng. **197**, 4429–4443 (2008)
72. Šmilauer, V. et al.: Yade Documentation 3rd ed. The Yade Project, (2021). 10.5281/zenodo.5705394
73. Cundall, P., Strack, O.: A discrete numerical model for granular assemblies. Géotechnique **29**(1), 47–65 (1997)
74. Cundall, P., Hart, R.: Numerical modelling of discontinua. Eng. Comput. **9**, 101–113 (1992)
75. Tomporowski, D., Nitka, M., Tejchman, J.: Application of the 3D DEM in the modelling of fractures in pre-flawed marble specimens during uniaxial compression. Eng. Fract. Mech. **277**, 108978 (2023)
76. Widulinski, L., Tejchman, J., Kozicki, J., Leśniewska, D.: Discrete simulations of shear zone patterning in sand in earth pressure problems of a retaining wall. Int. J. Solids Struct. **48**(7–8), 1191–1209 (2011)
77. Kozicki, J., Niedostatkiewicz, M., Tejchman, J., Mühlhaus, H.-B.: Discrete modelling results of a direct shear test for granular materials versus FE results. Granular Matter **15**(5), 607–627 (2013)
78. Kozicki, J., Tejchman, J., Műhlhaus, H.-B.: Discrete simulations of a triaxial compression test for sand by DEM. Int. J. Num. Anal. Meth. Geomech. **38**, 1923–1952 (2014)
79. Kozicki, J., Tejchman, J.: Relationship between vortex structures and shear localization in 3D granular specimens based on combined DEM and Helmholtz-Hodge decomposition. Granular Matter **20**, 48 (2018)
80. Suchorzewski, J., Tejchman, J., Nitka, M., Bobinski, J.: Meso-scale analyses of size effect in brittle materials using DEM. Granular Matter **21**(9), 1–19 (2019)
81. Nitka, M., Tejchman, J.: Meso-mechanical modelling of damage in concrete using discrete element method with porous ITZs of defined width around aggregates. Eng. Fract. Mech. **231**, 107029 (2020)
82. Reynolds, O.: An experimental investigation of the circumstances which determine whether the motion of water shall be direct or sinuous, and of the law of resistances in parallel channels. Phil. Trans. Roy. Soc London **174**, 935–982 (1883)
83. Batchelor, G.: An Introduction to Fluid Dynamics. Cambridge University Press, Cambridge (2000)
84. Tejchman, J., Bobinski, J.: Continous and discountinous modelling of fracture in concrete using FEM. Springer-Verlag, Berlin Heidelberg (2013)
85. Hökmark, H., Lönnqvist, M., Fälth, B.: Technical Report TR-10–23: THM-issues in repository rock–thermal, mechanical, thermo-mechanical and hydro-mechanical evolution of the rock at the Forsmark and Laxemar sites. SKB–Swedish Nuclear Fuel and Waste Management Co., 210; pp.26–27 (2010)
86. Barmak, I., Gelfgat, A., Vitoshkin, H., Ullmann, A., Brauner, N.: Stability of stratified two-phase flows in horizontal channels. AIP Phys. Fluids **28**, 044101 (2016)

87. Mathias, P.M., Naheiri, M., Oh, E.M.: A Density Correction for the Peng-Robinson Equation of State. In: Fluid Phase Equilibria, pp. 77–87. Elsevier Science Publishers B.V., Amsterdam (1989)
88. Peneloux, A., Rauzy, E., Freze, R.: A Consistent Correction for Redlich-Kwong-Soave Volumes. Fluid Phase Equilib. **8**, 7–23 (1982)